Cell

Article

Structural basis of poxvirus fusion regulation and anti-A16/G9 antibody-mediated neutralization and protection

Graphical abstract

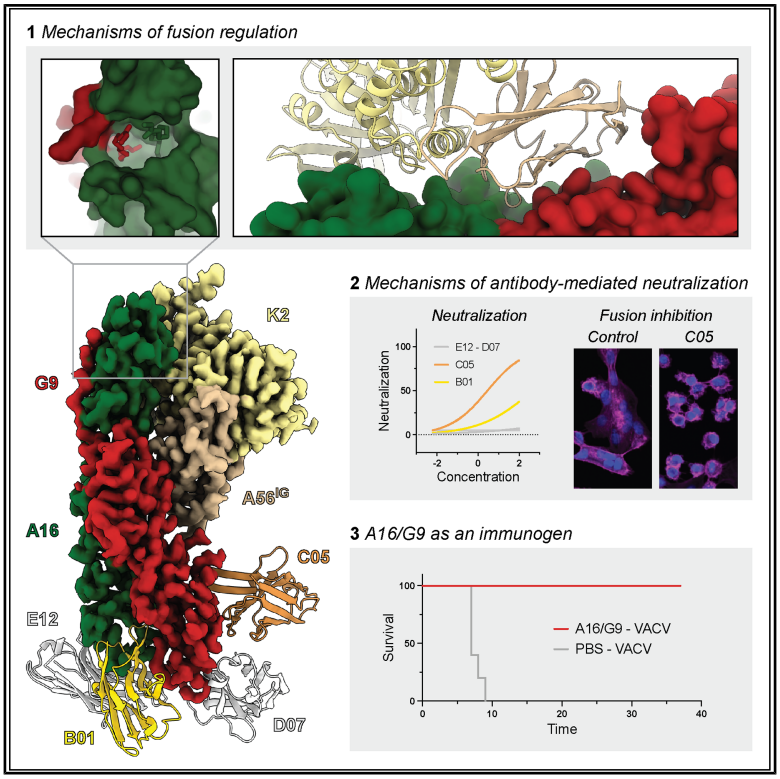

Highlights

- A56/K2 regulates viral fusion by binding to the N-terminal domains of A16 and G9
- The N-terminal domain of A16 contains a conserved myristoyl-binding pocket
- mAbs targeting A16/G9 block fusion and cross-neutralize VACV and several MPXV strains
- Immunization with A16/G9 protects mice from VACV infection

Authors

Annalisa Meola, Riccardo Vernuccio, Leandro Battini, ..., Juan Garcia-Arriaza, Olivier Schwartz, Pablo Guardado-Calvo

Correspondence

guardado@pasteur.fr

In brief

Since 2022, several strains of the monkeypox virus adapted to human-to-human transmission have emerged and raised international alarm, highlighting the need for new treatments. We studied A16/G9, a conserved complex involved in viral entry, and found that antibodies targeting this complex block fusion and neutralize MPXV. Mice immunized with the protein elicit a protective immune response. These findings pave the way to develop better vaccines and antivirals. Structural analysis of the poxvirus A16/G9 fusion complex reveals how antibodies block viral entry, providing a new target for vaccines and antivirals against mpox and related viruses.

Meola et al., 2025, Cell *188*, 1–17
October 30, 2025
https://doi.org/10.1016/j.cell.2025.07.040

CellPress

Please cite this article in press as: Meola et al., Structural basis of poxvirus fusion regulation and anti-A16/G9 antibody-mediated neutralization and protection, Cell (2025), https://doi.org/10.1016/j.cell.2025.07.040

Cell

CellPress
OPEN ACCESS

Article

Structural basis of poxvirus fusion regulation and anti-A16/G9 antibody-mediated neutralization and protection

Annalisa Meola,[1,14] Riccardo Vernuccio,[1,14] Leandro Battini,[1,14] Guillermo Albericio,[2] Pilar Delgado,[2] Rebecca Bamford,[3,4] Laura Pokorny,[3,4] Manon Broutin,[5] Alejandro Martínez León,[7] Sébastien Gallien,[8] María Gil,[2] María A. Noriega,[2] Florence Guivel-Benhassine,[9,10] Françoise Porrot,[9,10] Jeanne Postal,[9,10] Julian Buchrieser,[9,10] Mathieu Hubert,[9,10] Ahmed Haouz,[11] Pierre Lafaye,[12] Mariano Esteban,[2] Jochen S. Hub,[7] Matthieu Mahévas,[5,6] Pascal Chappert,[5] Jason Mercer,[3] Juan Garcia-Arriaza,[2,13] Olivier Schwartz,[9,10] and Pablo Guardado-Calvo[1,15,*]

[1]Structural biology of infectious diseases G5+ unit, Institut Pasteur, Université Paris Cité, Paris, France
[2]Department of Molecular and Cellular Biology, Centro Nacional de Biotecnología, Consejo Superior de Investigaciones Científicas (CNB-CSIC), Madrid, Spain
[3]Institute of Microbiology and Infection, School of Biosciences, University of Birmingham, Birmingham, UK
[4]Medical Research Council, LMCB, University College London, London WC1E 6BT, UK
[5]Institut Necker Enfants Malades (INEM), Université Paris Cite, INSERM U1151/CNRS UMR 8253, Action thématique incitative sur programme-Avenir, Team Auto-Immune and Immune B cells, Paris, France
[6]Université Paris Est-Creteil, Institut Mondor de Recherche Biomédicale (IMRB), INSERM U955, Team 2, Créteil, France
[7]Theoretical Physics and Center for Biophysics, Saarland University, Saarbrücken, Germany
[8]Service de Maladies Infectieuses, Centre Hospitalier Universitaire Henri Mondor, AP-HP, Université Paris Est Créteil (UPEC), Créteil, France
[9]Virus and Immunity Unit, Institut Pasteur, Université Paris Cité, Paris, France
[10]Vaccine Research Institute, Créteil, France
[11]Crystallography Platform-C2RT, Institut Pasteur, CNRS UMR3528, Université de Paris, Paris, France
[12]Antibody Engineering Platform, C2RT, Université de Paris Cité, CNRS UMR 3528, Institut Pasteur, 75015 Paris, France
[13]Centro de Investigación Biomédica en Red de Enfermedades Infecciosas (CIBERINFEC), Madrid, Spain
[14]These authors contributed equally
[15]Lead contact
*Correspondence: guardado@pasteur.fr
https://doi.org/10.1016/j.cell.2025.07.040

SUMMARY

Monkeypox virus (MPXV) is a poxvirus endemic to Central and West Africa with high epidemic potential. Poxviruses enter host cells via a conserved entry-fusion complex (EFC), which mediates viral fusion to the cell membrane. The EFC is a promising therapeutic target, but the absence of structural data has limited the development of fusion-inhibiting treatments. Here, we investigated A16/G9, a subcomplex of the EFC that controls fusion timing. Using cryo-electron microscopy, we showed how A16/G9 interacts with A56/K2, a viral fusion suppressor that prevents superinfection. Immunization with A16/G9 elicited a protective immune response in mice. Using X-ray crystallography, we characterized two neutralizing antibodies and engineered a chimeric antibody that cross-neutralizes several poxviruses more efficiently than 7D11, the most potent antibody targeting the EFC described to date. These findings highlight the potential of A16/G9 as a candidate for subunit vaccines and identify regions of the EFC as targets for antiviral development.

INTRODUCTION

Orthopoxviruses (OPXVs) are a group of enveloped DNA viruses that include important human pathogens, such as variola (VARV) and monkeypox (MPXV) viruses, the causative agents of smallpox and mpox, respectively. The prototypical OPXV is vaccinia virus (VACV), which was used to eradicate smallpox. Since smallpox vaccination was discontinued more than 40 years ago, herd immunity has waned, raising concerns about VARV reintroduction as a bioweapon or the emergence of zoonotic OPXVs. Global attention now focuses on mpox, a zoonosis causing recurrent and deadly outbreaks in Central and West Africa and recently spreading to non-endemic regions. In 2022 and 2024, the World Health Organization (WHO) has declared mpox a public health emergency of international concern (PHEIC), particularly due to the emergence of human-adapted MPXV strains.[1] Few options exist for mpox prevention and treatment. Attenuated vaccines confer protection but are expensive and do not induce long-term immunity.[2] Tecovirimat, an antiviral approved to treat smallpox and mpox, is active against

human-adapted MPXV strains[3,4] but has a low barrier to resistance,[5] and clinical trials showed no accelerated recovery.[6] Therefore, novel prophylactic and therapeutic strategies are urgently needed.

Enveloped viruses require fusion of viral and cellular membranes to enter host cells, a process mediated by surface proteins termed fusion complexes, which are prime targets for vaccines and antivirals. OPXVs produce two enveloped virion forms, mature virions (MVs) and extracellular virions (EVs), both using the same entry-fusion complex (EFC) for membrane fusion. Due to a lack of similarity with other viral fusion machineries, the mechanisms of action of the EFC remain largely unknown. The EFC is composed of 11 transmembrane proteins, three of which (L1, A16, and G9) are myristoylated.[7] The genetic repression of any of the EFC subunits results in the formation of morphologically normal virions that are incompetent for fusion.[8] Three stable subcomplexes have been identified: A28/H2,[9] A16/G9,[10] and G3/L5.[11] Unlike other enveloped viruses, OPXVs encode fusion suppressor proteins that interact with the EFC to control the timing and localization of viral fusion. One of them is the complex A56/K2, which is formed by a membrane protein (A56) and a serine-protease inhibitor (K2). Upon infection, A56/K2 forms a complex on the surface of infected cells, preventing superinfection and syncytium formation by targeting the subcomplex A16/G9. Viruses lacking A56 or K2, or with mutations in G9, generate large syncytia at neutral pH upon infection.[12,13] The structural basis of the A56/K2-mediated fusion inhibition remains unknown.

Antibodies targeting fusion complexes can block fusion and neutralize viral infection,[14–17] providing important clues for the development of antivirals and vaccines. However, the immunogenicity of different subunits of the EFC has not been systematically studied, and only L1 is known to elicit neutralizing antibodies (nAbs) that block fusion.[18–20] To investigate A16/G9 immunogenicity, we used VHHs, which are the variable domains of single-chain antibodies produced in camelids.[21] VHHs are smaller (15 kDa) than conventional Fabs (50 kDa), can target epitopes that are inaccessible to conventional antibodies, are easier to produce, are more thermostable, and can be engineered to produce multivalent antibodies.

Here, we produced a recombinant A16/G9 complex and confirmed its native conformation by performing binding assays and cryo-electron microscopy (cryo-EM) studies with the fusion suppressor A56/K2. To study its immunogenicity, we immunized an alpaca and isolated four non-competing VHHs, two of which block fusion and cross-neutralize several OPXVs. Using X-ray crystallography, we obtained their structures in complex with A16/G9 and engineered a bispecific, chimeric antibody comprising a neutralizing VHH and a stabilized A56/K2 complex, which potently neutralized VACV and MPXV. Prophylactic administration of this bispecific antibody in mice reduced VACV lung titers but did not result in a clear protective effect *in vivo*. However, mice immunized with A16/G9 elicited robust humoral responses that conferred complete protection against a lethal VACV challenge. Notably, modified vaccinia virus Ankara (MVA)-vaccinated mice fail to induce A16/G9-specific antibodies, whereas some smallpox vaccinees retained long-lived A16/G9-specific antibodies. These findings demonstrate that A16/G9 elicits cross-neutralizing and protective immune responses, supporting its inclusion into subunit vaccines and revealing targetable A16/G9 regions for antiviral development.

RESULTS

Structure of the A56/K2 fusion suppressor

A56 is a membrane protein composed of a conserved immunoglobulin (IG)-like domain ($A56^{IG}$), a variable stalk domain ($A56^{ST}$), and a C-terminal transmembrane anchor. K2 is a secreted serine-protease inhibitor (serpin) that requires association with A56 for its membrane localization (Figure 1A). How the two proteins interact is not known, but mutants destabilizing $A56^{IG}$ fail to inhibit viral fusion,[22] suggesting that $A56^{IG}$ binds K2. To explore this interaction, we generated a stable Drosophila Schneider S2 cell line that co-secreted $A56^{IG}$ and K2 from VACV. Using affinity and size-exclusion chromatography (SEC), we purified a stable $A56^{IG}$/K2 complex (70 kDa) (Figure 1B) and solved its crystal structure (Table S1; Figure 1C).

The structure revealed a 1:1 complex with $A56^{IG}$ bound to the K2 region formed by helices hD and hE, conserved across OPXVs (Figure S1). Structural analysis showed that K2 shares strong structural and sequence similarity to plasminogen activator inhibitor-1 (PAI-1), a key serpin involved in fibrinolysis regulation (Figure S2A). Like PAI-1, which transitions to an inactive latent conformation in the absence of an allosteric regulator,[23] the structure of K2 revealed a serpin fold in a latent conformation, with the uncleaved reactive center loop (RCL) inserted into β-sheet A. Molecular modeling suggested that the active conformation of K2 could also accommodate $A56^{IG}$ binding (Figure 1D). The N-glycans of $A56^{IG}$ extended away from the $A56^{IG}$/K2 interface (Figure S2B) and did not contribute to stabilizing the interaction (Figure S2C).

We conducted SDS-PAGE analysis to investigate the interaction of the recombinant K2 with urokinase-type plasminogen activator (uPA), the natural substrate of PAI-1. As a control, we used a stabilized mutant of PAI-1 (W175F) (Figure 1E). We observed that PAI-1 formed a covalent inhibitory complex with uPA, which could be distinguished from the small fraction of unreactive or latent PAI-1. By contrast, the recombinant K2 expressed in S2 cells, either alone or complexed with $A56^{IG}$, remained inactive, likely due to spontaneous conversion to a latent form during prolonged accumulation in insect cell culture.

Structure of A56/K2 in complex with A16/G9

A16 and G9 are paralogous proteins with the same domain organization: N- and C-terminal domains (NTD and CTD, respectively), a membrane-proximal region (MPR), and a transmembrane segment (Figures 2A, S3A, and S4). A16 includes a linker between the NTD and CTD and a short C-terminal tail, while G9 possesses an extended N-terminal tail important for the stabilization of the complex.[24] We cloned the NTD and CTD of both proteins from VACV into a bicistronic plasmid in frame with signal peptides to target them to the secretory pathway. Since the native complex remains unglycosylated in the virus, we mutated all potential N-glycosylation sites to avoid artificial modifications that could mask key regions (Figure S3B). We co-purified the

Please cite this article in press as: Meola et al., Structural basis of poxvirus fusion regulation and anti-A16/G9 antibody-mediated neutralization and protection, Cell (2025), https://doi.org/10.1016/j.cell.2025.07.040

CellPress
OPEN ACCESS

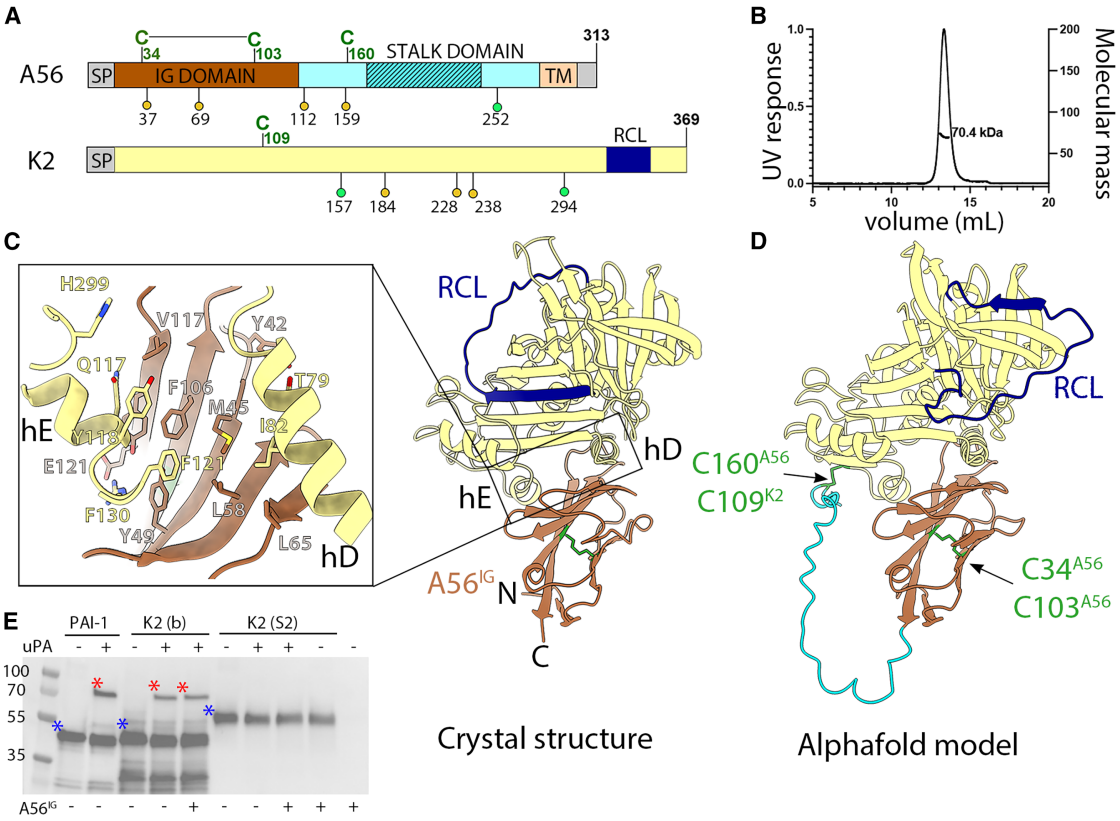

Figure 1. Structure of the fusion suppressor A56/K2

(A) Domain organization of A56 and K2, colored according to domains: signal peptide (SP), transmembrane segment (TM), and reactive center loop (RCL). The dashed area indicates an O-glycosylated region. N-glycosylation sites are shown as colored spheres below the diagram, orange if conserved, and green otherwise. Cysteines are indicated as a green "C" on the diagram.

(B) SEC-MALS analysis of the A56^{IG}/K2 complex.

(C) Crystal structure of A56^{IG}/K2 colored as in (A). Disulfide bonds are depicted as green sticks. The left panel provides a close-up view of the protein interface, with key residues depicted as sticks and labeled.

(D) AlphaFold2 model of the A56/K2 complex. K2 is in the active conformation, with the RCL exposed. The program predicts a disulfide bond between the two proteins.

(E) Western blot analysis of covalent complexes with uPA. Samples containing K2 expressed in bacteria (b), insect cells (S2), or PAI-1, either alone or combined with uPA or A56^{IG}, as indicated, were analyzed by western blot using an anti-strep antibody. Lane 1 shows protein markers. The covalent complexes (serpin/uPA) and free serpin are indicated by red and blue asterisks, respectively.

See also Figures S1 and S2.

proteins from the supernatant of transfected S2 cells and obtained a stable A16/G9 heterodimer (rA16/G9) (Figure S5).

To validate that rA16/G9 adopts the same conformation as on the viral surface, we studied its interaction with A56^{IG}/K2 (Figures 2B and S5). We observed that the complexes interacted strongly at neutral pH but weakly in the acidic solution, consistent with biological data showing that A56/K2-mediated fusion inhibition is sensitive to acidic conditions.[12] Neither rA16/G9 nor A56^{IG}/K2 dissociated across the pH range tested (Figure S5). To study whether an acidic environment induces conformational changes in rA16/G9, we crystallized rA16/G9 at pHs 7.5, 6.5, and 5.5. All structures were virtually identical, with root mean square deviations between C-alpha atoms of equivalent residues (rmsd) of 0.1–0.2 Å, suggesting that the reduced binding affinity at acidic pH does not result from major conformational changes (Figure 2B).

To uncover the structural determinants of the interaction between rA16/G9 and A56^{IG}/K2, we reconstituted the hetero-tetramer at neutral pH and performed single-particle cryo-EM, obtaining a 3.2 Å resolution reconstruction that showed clear density for the four components of the complex (Table S2; Figures 2C and S6). The final model showed that A16/G9 and A56^{IG}/K2 did not undergo conformational changes upon complex formation. As in the crystal structure, K2 displayed a latent conformation, with the RCL oriented away from the interaction interface with A16/G9, consistent with previous results indicating that RCL mutations did not affect fusion inhibition.[25] To investigate potential conformational changes at acidic pH, we collected another dataset at pH 5.5, obtaining a map at 4 Å resolution that showed no significant differences compared with neutral pH. We then analyzed the surface electrostatic potentials of the interfaces. Electrostatic analysis revealed mild and complementary charge distributions at neutral pH

Please cite this article in press as: Meola et al., Structural basis of poxvirus fusion regulation and anti-A16/G9 antibody-mediated neutralization and protection, Cell (2025), https://doi.org/10.1016/j.cell.2025.07.040

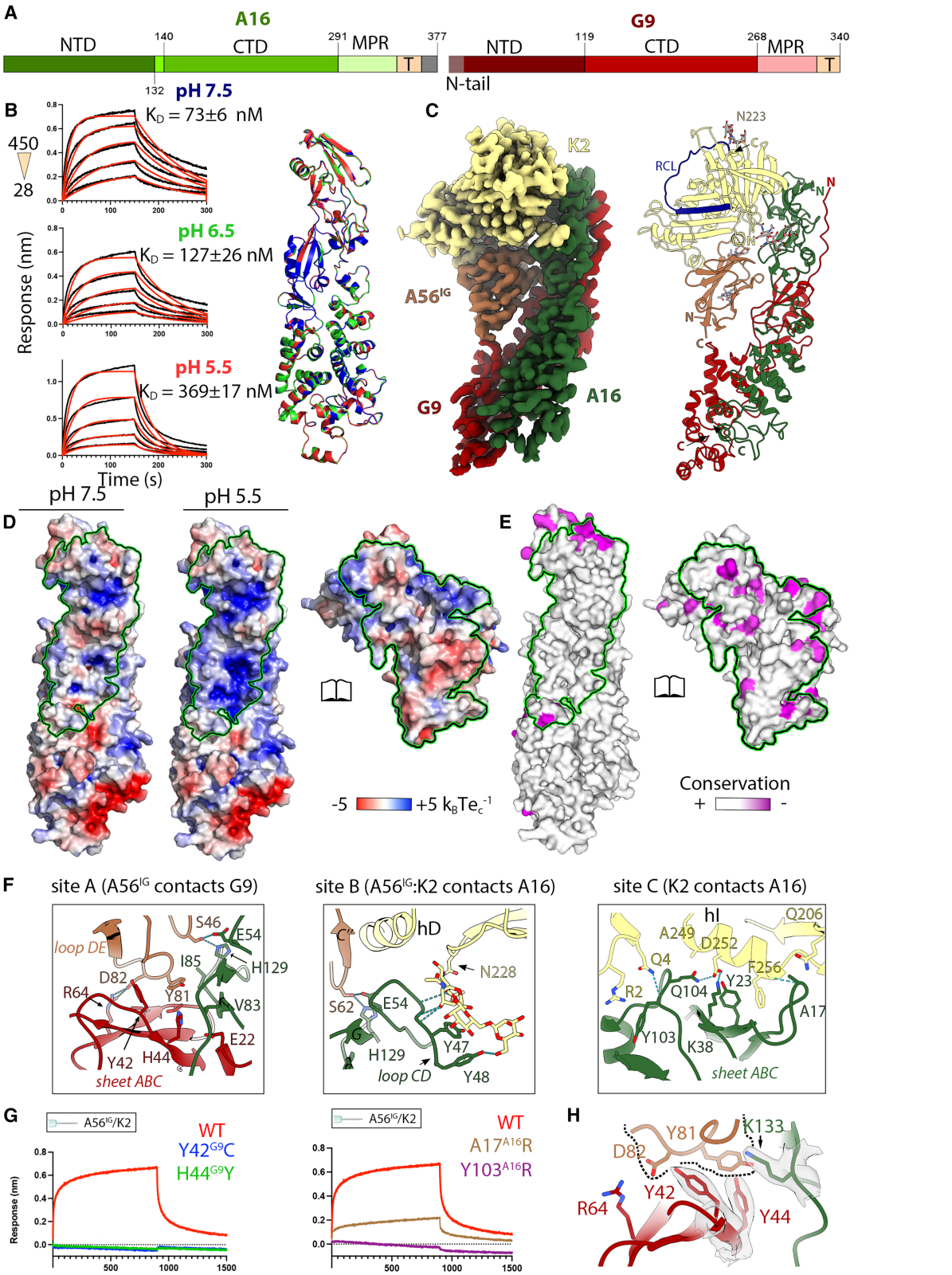

(legend on next page)

Please cite this article in press as: Meola et al., Structural basis of poxvirus fusion regulation and anti-A16/G9 antibody-mediated neutralization and protection, Cell (2025), https://doi.org/10.1016/j.cell.2025.07.040

(Figure 2D), but at acidic pH, the interface on A16/G9 became positively charged, decreasing electrostatic complementarity and explaining complex destabilization.

The structure of the hetero-tetramer revealed that A56^{IG}/K2 recognizes both NTDs of the A16/G9 heterodimer (Figures 2C, 2E, S1, S3A, and S4A). K2 contacts A16, while A56^{IG} contacts both A16 and G9 subunits. We identified three main contact sites (Figure 2F): (1) site A is centered around the *DE*^{A56} loop, which contacts Y42^{G9}, H44^{G9}, R64^{G9}, and I85^{A16}; (2) site B is centered around the N-glycan attached to N228^{K2}, which contacts Y47^{A16} and Y48^{A16}; and (3) site C comprises interactions between the α-helix I^{K2} and the N terminus of K2, which contacts A17^{A16}, Y23^{A16}, K38^{A16}, and Y103^{A16}. All these residues are conserved across OPXVs. To validate the structure and assess the contribution of A16 and G9 to the stability of the complex, we performed mutagenesis studies. Two independent studies[12,13] identified three mutations at site A (Y42C^{G9}, H44Y^{G9}, and H44R^{G9}) that overcome A56/K2-based membrane fusion inhibition. To determine whether these mutations affected the interaction with A56^{IG}/K2, we generated rA16/G9^{Y42C} and rA16/G9^{H44Y}. Both mutant complexes eluted in SEC-MALS as the wild-type (WT) complex, but neither of them interacted with A56^{IG}/K2 (Figure 2G). The crystal structure of rA16/G9^{H44Y} (Table S1) revealed that Y44^{G9} formed a hydrogen bond with K133^{A16} and occupied the space of Y81^{A56}, thereby preventing the interaction of A16/G9 with A56/K2 (Figure 2H). No adaptive mutations were identified on A16, so we engineered two: Y103R^{A16} and A17R^{A16}. The C-beta of Y103^{A16} is within 5 Å of R2^{K2}, so the Y103R mutation is expected to create steric constraints and electrostatic repulsion between the two arginines. The side chain of A17^{A16} is oriented toward the helix hI, so the mutation A17R^{A16} is expected to introduce steric constraints. We introduced each mutation separately into rA16/G9 and performed binding studies with A56^{IG}/K2 at neutral pH. We found that A17R^{A16} significantly reduced A56^{IG}/K2 binding, while Y103R^{A16} completely prevented the interaction (Figure 2G).

The NTD of A16 contains a conserved myristoyl-binding pocket

The structure of A16/G9 revealed a large hydrophobic cavity at the tip of the A16^{NTD} that might host the conserved N-terminal myristoyl groups of A16 and G9. This cavity is empty in the cryo-EM and X-ray crystallography maps because the recombinant proteins were not myristoylated. However, AlphaFold3[26] predicted the insertion of two myristic acid chains into the pocket, and atomistic molecular dynamics (MD) simulations confirmed that both N-myristates remained stably inserted into the pocket over a 2 μs simulation (Figure 3A). Comparison with the X-ray crystallography and cryo-EM models suggested that myristate insertion slightly shifts the AB loop and helix 3 (Figure S4B).

To understand the functional roles of G9 and A16 myristates in membrane fusion, we introduced glycine-2 to alanine (G2A) point mutations into recombinant VACV to generate myristate-null mutants. G2A mutants in G9 (G2A^{G9}), A16 (G2A^{A16}), or both (G2A^{G9}:G2A^{A16}) were viable, while the L1 G2A mutant (G2A^{L1}) was unviable, as previously reported.[27] We measured the growth kinetics of the viable mutants by infecting BSC-40 cells with WT, G2A^{G9}, G2A^{A16}, or G2A^{G9}:G2A^{A16} viruses at a multiplicity of infection (MOI) of 0.1 plaque-forming units (PFUs) per cell and determined the viral yield between 8 and 48 h post-infection (hpi). We observed a 3.3-fold reduction in viral yield at 8 hpi for the double-mutant G2A^{G9}:G2A^{A16}, but titers were comparable to WT at later time points (Figure 3B).

As repression of A27, a non-EFC protein, leads to fusion defects despite normal 24-hr viral yields,[8] we investigated if G9 and A16 G2A mutants exhibited similar entry defects. Thus, we infected HeLa cells with WT, G2A^{G9}, G2A^{A16}, or G2A^{G9}:G2A^{A16} and analyzed the mRNA expression of the early gene C11R by qRT-PCR (Figure 3C). We observed a 10% reduction in early gene expression for G2A^{G9} and G2A^{A16} and a 50% reduction for G2A^{G9}:G2A^{A16}, suggesting that G2A^{G9}:G2A^{A16} is unable to enter host cells as efficiently as WT. Next, we investigated whether the myristate-null mutants can induce cell-cell fusion at acidic pH using fusion-from-without assays. Like the WT virus, G2A^{G9} and G2A^{A16} induced cell-cell fusion at pH 5, resulting in the formation of multinucleated syncytia. However, G2A^{G9}:G2A^{A16} was much less efficient, resulting in a 10-fold reduction in its fusion index compared with WT (Figure 3D).

Antibodies targeting A16/G9 block fusion and cross-neutralize OPXV infection

To assess whether rA16/G9 elicits a neutralizing response, we immunized an alpaca with rA16/G9, generated a B cell-derived

Figure 2. Structure of A56^{IG}/K2:A16/G9 complex

(A) Domain organization of A16 and G9: N-terminal domain (NTD), C-terminal domain (CTD), membrane-proximal region (MPR), and transmembrane (T) segment.

(B) The left panels are BLI-sensorgrams showing binding kinetics of rA16/G9 to A56^{IG}/K2 at different pHs. The concentrations and pHs used in the experiment are indicated. Data are mean ± SD from three independent experiments (n = 3). The right panel shows the superimposed structures of rA16/G9 obtained at pH 7.5 (blue), 6.5 (green), and 5.5 (red).

(C) Cryo-EM density and final model of the A56^{IG}/K2:A16/G9 complex colored according to the proteins, as indicated.

(D) Open book representation of the surface electrostatic potentials of the complexes at pH 7.5 and 5.5, with negative and positive potentials displayed and colored according to the bar underneath. Contact areas are outlined in green.

(E) Open book representation of the A56^{IG}/K2 and A16/G9 surfaces colored by conservation, as indicated in the bar underneath. Contact areas are outlined in green.

(F) Close-up views of the three main contact sites (A, B, and C) with the main residues depicted as sticks and labeled. Dashed lines indicate polar interactions at the interface.

(G) BLI-sensorgrams showing binding kinetics of rA16/G9 WT and different mutants to A56^{IG}/K2 at neutral pH.

(H) Close-up view of contact site A on the crystal structures of rA16/G9^{H44Y}. To visualize the clashes with A56, we have depicted the DE^{A56} loop in the figure enclosed with a dashed line to highlight that this loop has been modeled. The main residues involved in the interaction are depicted in sticks and labeled.

See also Figures S3, S4, S5, and S6.

Please cite this article in press as: Meola et al., Structural basis of poxvirus fusion regulation and anti-A16/G9 antibody-mediated neutralization and protection, Cell (2025), https://doi.org/10.1016/j.cell.2025.07.040

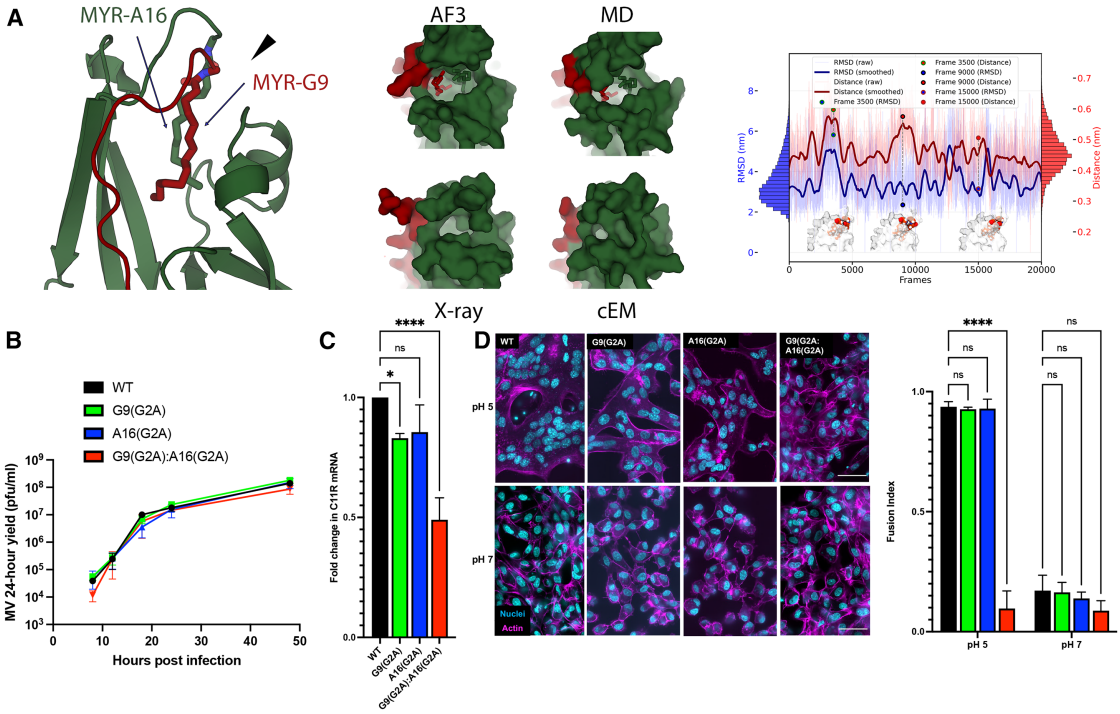

Figure 3. Myristoylation of G9 and A16 is required for syncytia formation

(A) The left panel displays a model of the myristoylated A16/G9 complex obtained from molecular dynamics (MD) simulations. A16 and G9 are colored green and red, respectively, with the two myristate groups indicated. The middle panel is surface representations of the pocket from the top, as indicated in the left panel with a black arrow. The right panel shows rmsd (blue) and distance (red) values between the center of mass of the two N-myristoylated glycine residues and the backbone atoms within 0.4 nm over simulation frames. Markers and inserts indicate values and structural configurations at frames 3,500, 9,000, and 15,000 (100 ps/frame).

(B) MV yield of WT and recombinant VACV on BSC-40 cells. Data are presented as mean values ± SD.

(C) Viral entry efficiency of WT and recombinant VACV. Data are presented as mean values ± SD. *p* values were determined by two-way ANOVA (Dunnett's test): NS, non-significant; **p* = 0.0321, *****p* < 0.0001.

(D) Cell-cell fusion experiments of WT and recombinant VACV. The left panels show representative images of the experiment, from which the fusion indices shown in the right panel have been calculated. Cells were fixed and stained for actin (phalloidin-594, magenta) and nuclei (Hoechst, cyan). Scale bar, 50 μm. Data are presented as mean values ± SD. *p* values were determined by two-way ANOVA (Sidak's test): NS, non-significant; *****p* < 0.0001.

See also Figure S4.

VHH phage display library, isolated four A16/G9-specific antibodies (B01, C05, D07, and E12), and produced them as monomeric VHHs and bivalent VHH-Fc, fused to human IgG1 Fc. ELISA-based competition assays and BioLayer Interferometry (BLI)-based binding experiments revealed binding to four different epitopes, with some cross-competition between B01 and E12 (Figure 4A), and suggested that B01 and E12 recognized a quaternary epitope (Figure 4B). Monomeric VHH-B01 neutralized VACV efficiently (IC_{50} = 160 nM), VHH-C05 and VHH-D07 were less potent (IC_{50} values of 1.6 and 3.6 μM, respectively), and VHH-E12 showed no neutralization (Figure S7A). Next, we evaluated the neutralization of the bivalent VHH-Fc using MV and EV forms of VACV (Figure 4C). Since VACV, MPXV, and other OPXVs produce proteins that inhibit complement activation and contribute to virulence,[28,29] we tested the Fc-fused VHHs with and without complement. We observed that C05-Fc strongly neutralized MVs (IC_{50} = 35 nM; 2.9 μg/mL), about 5 times better than the monomeric VHH-C05, and B01-Fc neutralized weaker (IC_{50} > 100 μg/mL), while E12-Fc and D07-Fc were inactive. Neither C05-Fc nor B01-Fc required complement for neutralization or neutralized the EV form. The differences between the monomeric and the bivalent formats are presumably due to steric and avidity effects. To assess cross-neutralization, we tested two strains of MPXV (clades Ib and IIb) (Figure 4D). C05-Fc and B01-Fc cross-neutralized both strains, E12-Fc showed weaker activity, and D07-Fc was inactive.

To investigate the structural basis for the binding and neutralization of these VHHs, we determined the crystal structures of rA16/G9 in complex with C05, B01, E12, and D07 (Table S1). In agreement with the BLI data, C05 and D07 bound to $G9^{CTD}$, whereas B01 and E12 targeted a quaternary $A16^{CTD}/G9^{CTD}$ epitope (Figure 5A). The epitope of C05 spans approximately 957 $Å^2$, with over half of the interactions mediated by CDR-3, which is inserted into a narrow cavity between α-6^{G9}, α-7^{G9}, and α-8^{G9}, close to the $A56^{IG}$/K2 binding region (Figure 5B). The epitope of D07 was buried 783 $Å^2$ and was mostly mediated by framework (FWR) residues that recognize a linear epitope on α-11^{G9} (aa 225–238) (Figure 5C). B01 inserts CDR1 and CDR3 into a cavity formed by α-6^{G9}, α-8^{G9}, α-9^{A16}, and α-13^{A16}, and

Please cite this article in press as: Meola et al., Structural basis of poxvirus fusion regulation and anti-A16/G9 antibody-mediated neutralization and protection, Cell (2025), https://doi.org/10.1016/j.cell.2025.07.040

CellPress
OPEN ACCESS

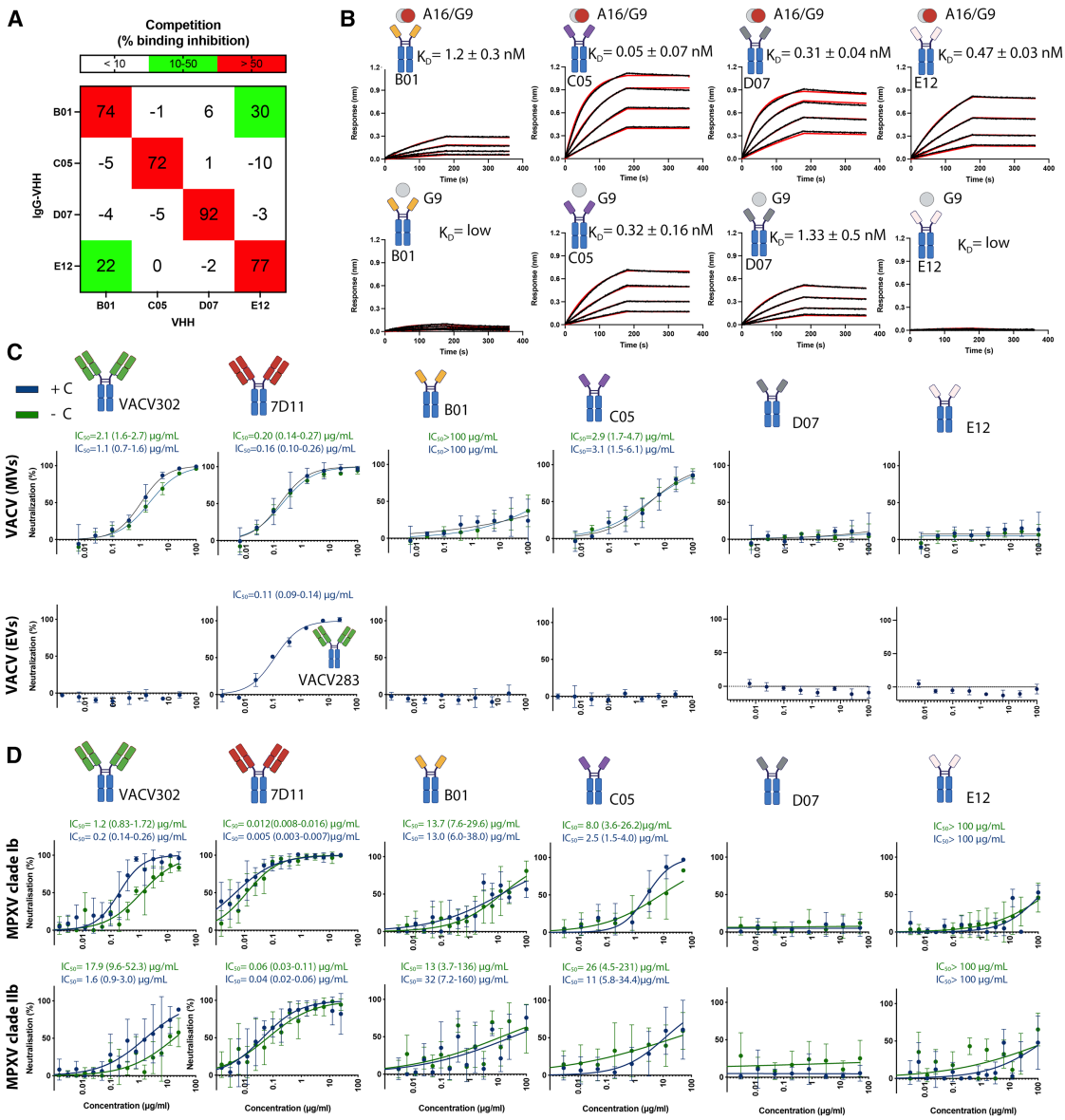

Figure 4. Antibodies targeting A16/G9 neutralize VACV and MPXV

(A) Competition ELISA of four VHHs. Competition is expressed as a percentage of blocking. A percentage above 50% suggests that the two VHHs bind at an overlapping epitope, and above 10% suggests partial interference.

(B) BLI-sensorgrams showing binding kinetics of rA16/G9 and G9 to the different VHH-Fc, as indicated.

(C) Neutralization assays with (blue lines) and without (green lines) complement (C) using VACV-MVs and EVs, as indicated. We include as controls two nAbs that do not require complement to neutralize the virus: 7D11 (α-L1[30]) and VACV-302 (α-A27[31]). Neutralization experiments with EVs were performed only in the presence of complement, and we used a nAb targeting B5 (VACV283) as a positive control. IC_{50} is the antibody concentration (µg/mL) for 50% neutralization. Data are mean ±95% confidence interval (CI) of triplicates from three independent experiments (n = 3).

(D) Neutralization assays using MPXV clade Ib and IIb, as indicated. Data are mean ±95% CI of triplicates from four independent experiments (n = 4).

See also Figure S7.

the loop between α-10^{A16} and α-11^{A16} (Figure 5D). The epitope of E12 was buried around 1,000 Å^2, equally distributed between A16 and G9. The antibody approaches the complex such that FWR residues bind α-10^{A16} and the loop between α-10^{A16} and α-11^{A16}, and CDR3 recognizes G9 close to the CTD termini (Figure 5E). Although the epitopes of B01 and E12 do not overlap, they both bind the loop between α-10^{A16} and α-11^{A16}, so the weak cross-competition we observed in the ELISA experiment may be due to each antibody stabilizing a different conformation of this loop, thereby altering the epitope of the other antibody.

To understand the mechanism of neutralization, we tested whether the antibodies interfered with virus adsorption. We

Please cite this article in press as: Meola et al., Structural basis of poxvirus fusion regulation and anti-A16/G9 antibody-mediated neutralization and protection, Cell (2025), https://doi.org/10.1016/j.cell.2025.07.040

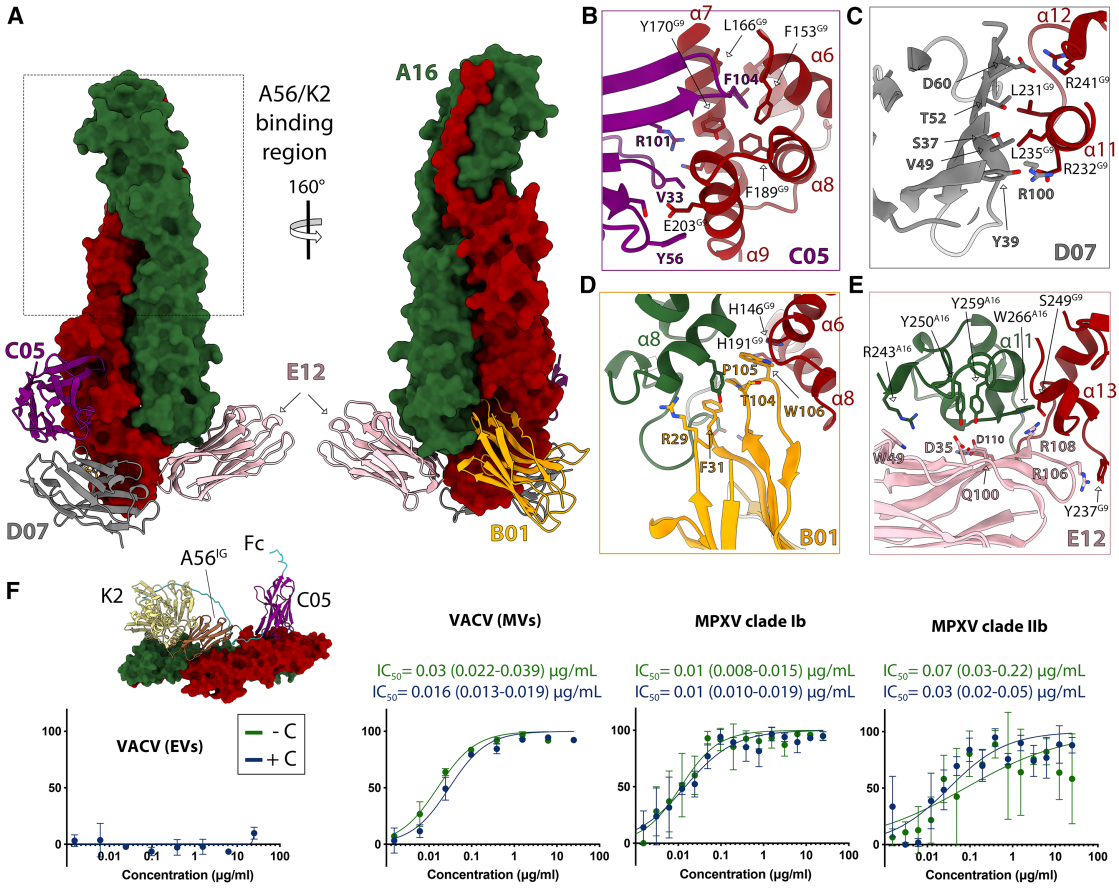

Figure 5. Structural-based design of a potent chimeric antibody

(A) Two rotated views of a model of rA16/G9 (A16 green, G9 red) bound to VHH-C05 (magenta), VHH-D07 (gray), VHH-B01 (yellow), and VHH-E12 (pink).

(B–E) Close-up views of the interfaces with VHH-C05 (B), VHH-D07 (C), VHH-B01 (D), and VHH-E12 (E). Each interface is shown in cartoon representation, with the most relevant interacting side chains depicted as sticks and labeled.

(F) The top panel is a model showing the design of the bispecific antibody A56^{IG}/K2/C05-Fc, with linkers (cyan) connected to the different domains. The bottom panels show neutralization assays of the bispecific antibody with/without complement (C) using VACV-MVs or EVs and MPXVs clade Ib and IIb, as indicated. Data are presented as mean values ±95% CI of triplicates from three independent experiments (n = 3).

See also Figure S7.

incubated virus-antibody mixtures with cells, washed off unattached particles, and measured residual virus using qPCR. None of the antibodies reduced virus-cell binding (Figure 6A). Next, we tested the effect of the antibodies on cell-cell fusion by adsorbing virus-antibody mixtures to cells and inducing cell-cell fusion by acidifying the media. As controls, we used 7D11, which targets the EFC protein L1, and LA5, which targets the non-EFC protein D8. As expected, 7D11 inhibited cell-cell fusion in a dose-dependent manner, while LA5 had no effect. Both B01-Fc and C05-Fc reduced cell-cell fusion, although C05-Fc was more efficient (Figure 6B), in line with their neutralizing activities. To evaluate the effect of the antibodies on VACV EV spread, we performed a comet tail inhibition assay. We added monoclonal antibodies (10 µg/mL) to the medium, infected the cells with VACV (IHD-J strain), and stained the cell monolayer with crystal violet 2 days later to visualize the "comets" produced by satellite plaques. Neither C05-Fc nor B01-Fc reduced EV spread (Figure 6C).

We next wondered whether we could use the structural information to engineer antibodies that neutralize better than 7D11, which is the most potent complement-independent nAb reported to date. First, as bivalent C05-Fc was more active than the monomeric form, we tested the neutralizing activity of a tetravalent antibody[32] containing two copies of C05 combined with two copies of B01 (C05-B01-IgG) or four copies of C05 (C05-C05-IgG) (Figure S7B). None of them neutralized VACV better than 7D11. Next, we postulated that a bispecific antibody combining VHH-C05 with an nAb targeting the A56/K2 binding region would neutralize the virus better. Since we did not identify an antibody targeting this region, we designed a bispecific antibody by fusing A56^{IG}/K2 to the N terminus of C05-Fc. This bispecific antibody (A56/K2/C05-Fc) neutralized VACV tenfold better than 7D11 and both strains of MPXV as effectively as 7D11, with or without complement (Figure 5F).

To investigate the mechanism of neutralization of the bispecific antibody, we performed functional assays. As for C05-Fc

Please cite this article in press as: Meola et al., Structural basis of poxvirus fusion regulation and anti-A16/G9 antibody-mediated neutralization and protection, Cell (2025), https://doi.org/10.1016/j.cell.2025.07.040

CellPress
OPEN ACCESS

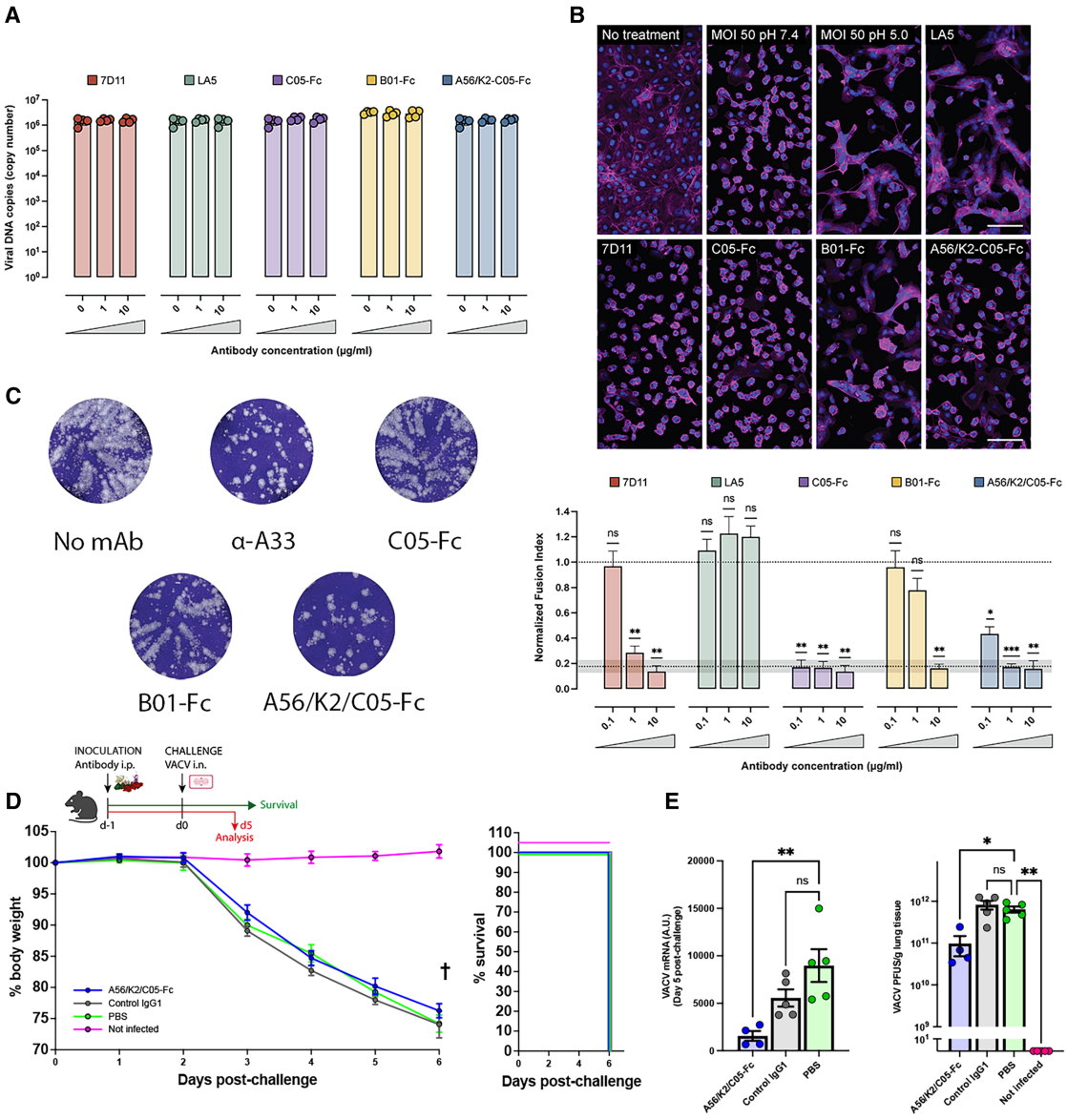

Figure 6. Functional characterization of monoclonal antibodies

(A) Adsorption assay evaluating mAb inhibition of VACV (WR strain) binding to BSC-40 cells. Bound viral particles were quantified using RT-qPCR to detect genomic DNA. We included 7D11 (α–L1) and LA5 (α–D8) as controls. Data are presented as averages ± SD from four independent experiments ($n = 4$).

(B) Fusion inhibition assay to evaluate the ability of the mAbs to inhibit VACV-mediated cell-cell fusion at acidic pH. Cells were fixed and stained for actin (phalloidin-594, magenta) and nuclei (Hoechst, cyan). Scale bar, 100 μm. The top panels show representative images of the experiment, from which the fusion indices shown in the bottom panel have been calculated. The dotted line below indicates the mean of the normalized fusion index at pH 7.4, and the gray band the SD of this mean. Data are presented as averages ± SD, with $n = 3$. p values were determined using a one-sample t test: NS, non-significant; $^{**}p$(7D11, 1 μg/mL) = 0.005, $^{**}p$(7D11, 10 μg/mL) = 0.0029, $^{**}p$(C05-Fc, 0.1 μg/mL) = 0.0044, $^{**}p$(C05-Fc, 1 μg/mL) = 0.0033, $^{**}p$(C05-Fc, 10 μg/mL) = 0.0033, $^{*}p$(B01-Fc, 10 μg/mL) = 0.0017, $^{*}p$(A56/K2/C05-Fc, 0.1 μg/mL) = 0.0102, $^{***}p$(A56/K2/C05-Fc, 1 μg/mL) = 0.0008, $^{**}p$(A56/K2/C05-Fc, 10 μg/mL) = 0.0057.

(C) Comet inhibition assay to evaluate the ability of the mAbs to inhibit VACV (IDH-J strain) spread. We used as positive control A20G2 (α–A33).

(D) *In vivo* prophylactic effect of A56^{IG}/K2/C05-Fc. We inoculated 100 μg of A56/K2/C05-Fc or an irrelevant monoclonal antibody or PBS in C57BL/6 mice ($n = 10$/group), and the following day we challenged the animals with a lethal intranasal dose (10^6 PFUs/mouse) of VACV (WR strain). Control animals were inoculated with PBS. We monitored changes in body weight (left panel) and survival rate (right panel). Data are presented as mean values ± SD.

(E) VACV mRNA levels (left panel) and infections virus (right panel) in the lungs of infected mice ($n = 5$/group) at day 5 post-infection. Data are presented as mean ± SD and represent one experiment with 5 mice per group.

Please cite this article in press as: Meola et al., Structural basis of poxvirus fusion regulation and anti-A16/G9 antibody-mediated neutralization and protection, Cell (2025), https://doi.org/10.1016/j.cell.2025.07.040

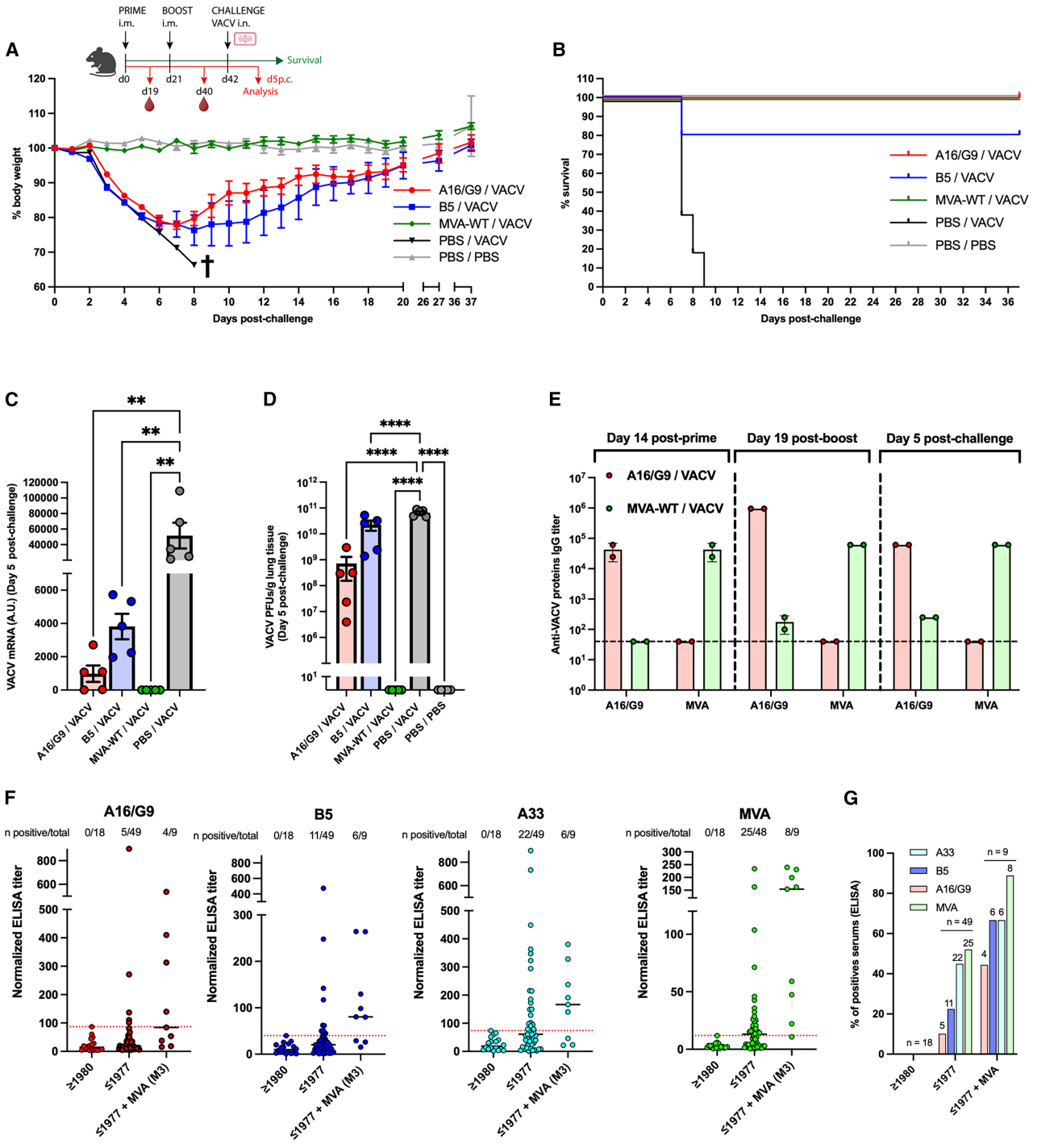

Figure 7. Immunization with rA16/G9 protects against lethal VACV challenge and induces specific antibodies

(A and B) Body weight loss (A) and survival (B) of C57BL/6 mice (n = 10/group) immunized with MVA, rA16/G9, or B5 ectodomain and challenged with VACV WR. Animals immunized with PBS and challenged with VACV WR were used as a positive control of infection, and naive mice inoculated with PBS were used as negative controls. Data are presented as mean ± SD.

(C) VACV mRNA levels assessed in the lungs of infected mice on day 5 post-infection. Data are shown as mean ± SD. p values were determined by ordinary one-way ANOVA (Tukey's test): NS, non-significant; $^{**}p$(A16/G9) = 0.0027, $^{**}p$(B5) = 0.0045, $^{**}p$(MVA) = 0.0023.

(D) VACV titers assessed in the lungs of infected mice on day 5 post-infection. Data are shown as mean ± SD. p values were determined by ordinary one-way ANOVA (Dunnett's test): NS, non-significant; $^{****}p < 0.0001$.

(legend continued on next page)

Please cite this article in press as: Meola et al., Structural basis of poxvirus fusion regulation and anti-A16/G9 antibody-mediated neutralization and protection, Cell (2025), https://doi.org/10.1016/j.cell.2025.07.040

and B01-Fc, the bispecific antibody had no effect on viral attachment to cells but reduced cell-cell fusion in a dose-dependent manner (Figures 6A and 6B). Although it did not neutralize EVs, it delayed spread, partially inhibiting comet formation (Figure 6C). To elucidate the cooperative mechanism between C05 and A56^{IG}/K2, we tested whether A56^{IG}/K2, either alone or in combination with C05-Fc, has the same activity as when A56^{IG}/K2 and C05 are fused through a linker (Figure S7C). A56^{IG}/K2 alone did not neutralize VACV and, when combined with C05-Fc, did not enhance its neutralization activity. These results suggest that the synergy observed in the bispecific antibody is due to cooperative binding, where the binding of C05 enhances the binding of A56/K2, thereby increasing neutralization.

We next evaluated the *in vivo* protective prophylactic efficacy of the bispecific antibody against VACV. We administered 100 μg of A56/K2-C05-Fc intraperitoneally to C57BL/6 mice (n = 10/group) 1 day prior to a lethal intranasal challenge with VACV (strain western reserve [WR]). We did not observe any protection, as all animals treated with A56/K2-C05-Fc lost body weight at a similar rate to PBS- and control antibody-treated infected groups and succumbed to infection by day 6 post-infection (Figure 6D). However, at day 5 post-challenge, we detected a significant reduction in VACV viral mRNA levels and infectious virus in the lungs of A56/K2-C05-Fc-treated mice compared with PBS- and control antibody-treated mice (Figure 6E), indicating that the bispecific antibody is partially inhibiting viral replication. This discrepancy between potent *in vitro* neutralization and limited *in vivo* efficacy has been previously reported for monoclonal antibodies targeting MV antigens[31] and highlights the challenges of achieving therapeutic protection through MV-directed antibodies alone.

Immunization with rA16/G9 confers full protection against lethal VACV challenge in mice

We evaluated the protective efficacy of rA16/G9 immunization in a murine model of lethal VACV infection. C57BL/6 mice (n = 10/group) were immunized intramuscularly twice (weeks 0 and 3) with MVA (10^7 PFUs/mouse), rA16/G9 (10 μg/mouse), or B5 ectodomain (10 μg/mouse). At week 6, mice were challenged intranasally with a lethal dose of 10^6 PFUs of VACV (strain WR) and monitored daily for body weight loss and survival for 5 weeks. As expected, PBS controls lost body weight and died within 7–9 days. MVA-immunized mice were fully protected, all survived, and no body weight loss nor clinical signs of disease were observed. Notably, all rA16/G9-immunized mice survived the VACV challenge, while B5 conferred 80% protection (Figures 7A and 7B). Mice immunized with rA16/G9 recovered weight faster and had lower lung VACV mRNA levels and infectious viral titers at day 5 post-infection than B5-immunized mice (Figures 7C and 7D).

Next, we compared humoral responses induced by MVA- and rA16/G9-vaccinated mice (Figure 7E). MVA-vaccinated mice, despite being protected, showed negligible A16/G9-specific IgG levels, even after boosting or VACV challenge. However, mice vaccinated with a single dose of rA16/G9 elicited significant levels of A16/G9-specific IgG antibodies, which increased after the second dose.

Detection of A16/G9-specific antibodies in humans

There are no previous studies evaluating human antibody responses to A16/G9. To investigate this, we examined whether first-generation smallpox vaccines induced A16/G9-specific antibodies and whether these responses could be boosted by MVA vaccination. Using ELISA, we measured antibody levels against A16/G9, B5, A33, and MVA proteins in human sera (Figure 7F). We established seropositivity thresholds based on a control panel of 18 serum samples from unvaccinated donors born after 1980. Upon screening 49 serum samples of vaccinated donors born before 1977, we found that 52% were seropositive for MVA, 45% for A33, 22% for B5, and 10% for A16/G9 (Figure 7G), although only two had high A16/G9 antibody titers. To assess whether this response could be enhanced by vaccination with the attenuated third-generation vaccine (MVA), we analyzed 8 sera from individuals born before 1977 and vaccinated with MVA between 2021 and 2024. In this cohort, 90% were seropositive for MVA, 66% for A33 and B5, and 44% for A16/G9, indicating that MVA can effectively recall A16/G9-specific responses.

DISCUSSION

Many emerging diseases are caused by enveloped viruses that rely on membrane fusion to enter host cells. This process is mediated by fusion proteins, which insert a fusion peptide/loop into host membranes to fuse them with the viral envelope. On the viral surface, fusion proteins form complexes with accompanying proteins, which are prime targets for nAbs and antivirals.[33] Here, we focused on the A16/G9 complex, the largest EFC subunit, and the region in which all viral fusion suppressors bind to regulate fusion timing. Using a combination of structural and functional assays, we revealed the structural basis of A56/K2-mediated fusion inhibition and mapped key epitopes that elicit nAbs. Given the high amino acid sequence similarity of A16/G9 across OPXVs, the conclusions extracted here are expected to be valid for all poxviruses, providing an excellent framework for understanding poxvirus fusion and developing effective antivirals and vaccines.

A major challenge in understanding poxvirus fusion is identifying which of the EFC proteins acts as the fusion protein, as none resemble a known viral fusion protein.[7] Sequence analysis indicated that only three EFC proteins (A16, G9, and L1) are conserved across the phylum,[34] and all are the targets of

(E) ELISA titers of A16/G9 (red) and MVA (green)-specific IgG in serum samples from immunized mice at three different times, as indicated. The x axis shows the immobilized proteins on the ELISA plates: the recombinant A16/G9 or an extract of cells infected with MVA. The y axis is the antibody titer of pool serum samples. Data are presented as mean values ± SD.

(F) ELISA titers of A33 (cyan), B5 (blue), A16/G9 (red), and MVA (green)-specific antibodies in the sera of individuals vaccinated against smallpox (born < 1977), not vaccinated (born > 1980), and vaccinees boosted with MVA-BN (<1977 + MVA).

(G) Number and frequency of seropositive individuals for each antigen in each group, as indicated.

proteins and antibodies that block fusion.[12,30,35] While none of the three display a classical fusion peptide/loop, all possess conserved N-myristoylated ends that may play a similar role. Treatment of VACV with an N-myristoylation inhibitor abrogates membrane fusion and infection, and mutagenesis studies show that the N-myristoyl group of L1 is essential for entry.[27]

Here, we show that $A16^{NTD}$ contains a hydrophobic cavity accommodating A16 and G9 N-myristoyl groups. Mutagenesis studies reveal that VACV tolerates the removal of one group, but a double myristate-null mutant is strongly impaired in cell-cell fusion and infectivity. G9 and A16 myristoylation may promote rapid membrane targeting and orientation, enhancing membrane fusion efficiency.[36] In the absence of G9 and A16 myristoylation, viral fusion occurs at a slower rate, relying on random contacts between the virus tip and the host membrane. Alternatively, A16 and G9 myristates may work in concert with that of L1, stabilizing membrane insertion and promoting viral fusion. MD simulations of influenza HA indicate that the membrane binding affinity of a single fusion peptide is approximately −40 kJ/mol.[37] As the estimated free energy required to form a stalk-like structure on a membrane is between −250 and −500 kJ/mol,[38] at least three HA trimers are needed to mediate fusion.[39] The membrane binding affinity of a single myristate is about −22 kJ/mol.[40] Therefore, assuming only the myristoyl groups insert into the membrane, at least 12 myristates, and thus four complexes, may be needed to prevent the fusion complex from dissociating during the fusion reaction. In the absence of G9 and A16 myristoylation, more fusion complexes are required, resulting in a slower fusion efficiency.

nAbs targeting fusion complexes block viral entry by preventing membrane insertion or the structural reorganizations required for membrane fusion.[14,16] A56/K2 might block fusion through either mechanism. As it binds near the myristoyl-binding pocket, it could block membrane insertion, but it may also prevent A16/G9 conformational changes or interactions with other EFC proteins. As there were no reported antibodies targeting either A16 or G9, we used the recombinant A16/G9 complex to immunize an alpaca. We isolated four VHHs, two of which (B01 and C05) neutralized VACV by blocking fusion. B01, which targets an epitope near the MPR, was more effective as a monomer, while C05, targeting an epitope near the A56/K2 binding site, was more effective when fused to an Fc. These differences suggest that regions closer to the MPR are partially buried on the viral particle, likely mediating interactions with other EFC proteins, while regions closer to the NTD are more exposed. Indeed, a model of the EFC obtained using AlphaFold[41] shows that the NTD regions of A16/G9 are fully exposed, while the CTD and especially the MPR are buried, in line with our observations. Alternatively, depending on the neutralization mechanism, it is possible that B01-Fc binds the EFC, as well as the monomer, but is less active. Both antibodies bind far from the myristoyl-binding pocket, indicating that they block fusion either by preventing A16/G9 or another protein of the EFC from undergoing conformational changes or by blocking the interaction of A16/G9 with another subunit of the EFC.

To assess protection by a single nAb targeting A16/G9, we engineered a bispecific antibody by fusing C05 and A56/K2 to a human Fc, which showed strong cross-neutralization and outperformed the benchmark nAb 7D11 *in vitro*. However, prophylactic administration of this bispecific antibody did not protect mice from lethal VACV challenge despite reducing viral load in lungs. This aligns with previous studies indicating that therapies based on monoclonal antibodies targeting only MVs did not confer protection against VACV and required combination with anti-EVs antibodies for full protection.[31]

The emergence of mpox has renewed interest in developing vaccines. Attenuated vaccines are safe and effective, but they are difficult to produce and do not confer long-term immunity.[2] Current mRNA-based vaccines protect animals[42–47] but elicit an immune response focused on a limited number of antigens. Only L1, and to a lesser extent A27, induce complement-independent nAbs. Since poxviruses encode complement inhibitors,[48–50] optimal vaccines should elicit potent, cross-reactive neutralizing responses in the absence of complement. Here, we showed that A16/G9 might elicit a complement-independent immune response as effective as that of L1. We also demonstrated that immunization with a recombinant A16/G9, lacking all N-glycosylation sites and the MPR regions, conferred full protection in mice against a lethal VACV challenge, outperforming the well-characterized B5 protein.

We and others[51] observed that MVA induced low anti-A16/G9 antibody levels in mice, and we investigated the immunogenicity of this complex in humans. Comparing the seropositivity rate and A16/G9-specific antibody titers between individuals born before 1977 (vaccinated) and those born after 1980, when the vaccination campaign ended, we found 10% of vaccinees retained A16/G9-specific antibodies more than 40 years after vaccination, although most had titers close to the cutoff. These were lower than for B5 or A33, suggesting that the initial response against A16/G9 is subdominant. Notably, L1, another component of the EFC that elicits a strong, complement-independent neutralizing response, is also poorly immunogenic,[52] suggesting that poxviruses have developed strategies to prevent the immune system from recognizing the EFC. Titers of B5-specific and A33-specific antibodies are boosted after multiple vaccinations.[52] Here, we corroborated these findings and found that seropositivity rates and antibody titers for A16/G9 increase when the immune response is boosted with the attenuated MVA years after the first vaccination, but these remain lower than those for B5 and A33.

Poxviruses remain a major public health problem. Despite this, only tecovirimat has been approved by regulatory agencies, and recent clinical trials question its efficacy, highlighting the need for new antivirals. Here, we performed a structural and functional analysis of A16/G9, demonstrating that A56/K2 blocks viral fusion by binding to the NTD domains of A16/G9. This finding highlights the regions to target for the development of fusion-blocking antivirals, like those described for HIV.[53] Overall, these findings will pave the way for the development of better subunit vaccines and antivirals targeting the fusion machinery.

Limitations of the study

Although A16/G9 immunization provided full protection against lethal VACV challenge, vaccinated mice still exhibited signs of disease. We tested only a single vaccination schedule, dose,

adjuvant, and platform, without evaluating combinations with EV antigens. Optimizing these parameters may improve A16/G9 efficacy and allow comparison with other combinations currently in clinical trials. Furthermore, while the murine model is widely used to study VACV infection and vaccination, additional *in vivo* studies, particularly in mpox models like CAST/EiJ mice or non-human primates, are needed to validate A16/G9 immunogenicity and protection.

RESOURCE AVAILABILITY

Lead contact

Further information and requests for resources and reagents should be directed to and will be fulfilled by the lead contact, Pablo Guardado-Calvo (guardado@pasteur.fr).

Materials availability

All unique/stable reagents generated in this study are available from the lead contact with a completed materials transfer agreement.

Data and code availability

Atomic coordinates of the complexes A16/G9/A56^{IG}/K2 (pH 8), A16/G9/A56^{IG}/K2 (pH 5.5), A56^{IG}/K2, A16/G9/D07/B01/C05, A16/G9/D07/E12, A16/G9H44Y/D07, A16/G9/D07 (pH 5.5), A16/G9/D07 (pH 6.5), and A16/G9/D07 (pH 7.5) have been deposited into the Protein Data Bank (PDB) and were assigned PDB IDs of 9HBK, 9RDH, 9HL2, 9HLS, 9HPA, 9HNG, 9R09, 9R0B, and 9R0J, respectively. The cryo-EM maps of the tetrameric complexes A16/G9/A56/K2 at neutral and acidic pHs have been deposited in the Electron Microscopy Data Bank (EMDB) and were assigned EMD codes 52019 and 53936, respectively. This paper does not report original code.

ACKNOWLEDGMENTS

We thank the staff of the Institut Pasteur crystallography facility, the PX1 and PX2 beamlines, the Polaris microscope at synchrotron SOLEIL (St. Aubin, France), and Diamond cryo-EM facilities. Access to Diamond was funded by iNEXT-Discovery/Instruct (PID: 25820, VID: 43499) and funded by the European Union Research and Innovation programme Horizon Europe (ISIDORe—grant agreement number 101046133). The NanoImaging Core Facility at Institut Pasteur is acknowledged for support with sample preparation, image acquisition, and analysis. The NanoImaging Core was created with the help of a grant from the French Government's Investissements d'Avenir program (EQUIPEX CACSICE - Centre d'analyse de systèmes complexes dans les environnements complexes, ANR-11-EQPX-0008). We also thank the CNB-CSIC animal facility for help and assistance, Marija Backovic for useful discussions on the serpin assay, and Pierre Legrand for facilitating rapid access to Polaris. The P.G.-C. lab is funded by the Institut Pasteur, the National French Research Agency (ANR; ANR-22-CE11-0003 and ANR-24-CE15-6625), and the European Union RESILIENCE-R-2023 (n°101168024). The O.S. lab is funded by Institut Pasteur, Fondation pour la Recherche Médicale (FRM), ANRS, the Vaccine Research Institute (VRI) (ANR-10-LABX-77), Labex IBEID (ANR-10-LABX-62-IBEID), the HERA projects DURABLE (grant 101102733), and LEAPS. J.P. is supported by DURABLE. The J.G.-A. lab is funded by CSIC grant 202120E079; grant CNS2022-135511 from the Spanish Ministry of Science, Innovation, and Universities (MCIU)/Spanish Research Agency (AEI)/10.13039/501100011033 and the European Union NextGenerationEU/PRTR to promote the consolidation of research; Centro de Investigación Biomédica en Red de Enfermedades Infecciosas (CIBERINFEC), co-financed with FEDER funds; and Spanish MCIU/AEI/10.13039/501100011033 grant PID2020-114481RB-I00. J.G.-A. and M.E. are also funded by the European Union RESILIENCE-R-2023 (n°101168024), funded by the European Union. Views and opinions expressed are those of the author(s) and do not necessarily reflect those of the European Union or the European Defence Fund. Neither the European Union nor the granting authority can be held responsible for them. This is related to the project RESILIENCE-R-2023 (n°101168024). J.S.H. and A.M.L. are funded by the European Union's Horizon 2020 research and the innovation program under Marie Sklodowska Curie Grant 860592 and Deutsche Forschungsgemeinschaft (DFG, German Research Foundation; grants SFB1027/B7 and INST256/539-1). The P.C. and M.M. lab is funded by the National French Research Agency (ANR-24-CE15-6625 and France 2030 funding ANR-24-CHBS-0003). L.P. was supported by the UCL Birkbeck MRC DTP. R.B. was funded by the MRC Laboratory for Molecular Cell Biology PhD program. J.M. was supported by the MRC Laboratory for Molecular Cell Biology (MC_UU_00012/7). The funders had no role in the study design, data collection and analysis, decision to publish, or manuscript preparation.

AUTHOR CONTRIBUTIONS

P.C., J.M., J.G.-A., O.S., and P.G.-C. conceptualized the study. A.M., R.V., L.B., G.A., P.D., R.B., L.P., M.B., A.M.L., M.G., M.A.N., F.G.-B., F.P., J.P., J.B., M.H., A.H., P.L., and P.G.-C. conducted the experiments. A.M., R.V., L.B., G.A., P.D., R.B., L.P., A.M.L., J.P., J.B., M.H., P.L., J.S.H., M.M., P.C., J.M., J.G.-A., O.S., and P.G.-C. analyzed the data. S.G. and M.M. provided access to human sera and metadata. J.S.H., P.C., J.S., J.G.-A., O.S., and P.G.-C. supervised the study. A.M., L.B., P.C., J.M., J.G.-A., O.S., and P.G.-C. wrote the manuscript. All authors interpreted the data, provided critical input, and revised the manuscript.

DECLARATION OF INTERESTS

A.M., M.H., O.S., and P.G.-C. have a patent application for poxvirus immunogens (PCT/EP2024/063801).

STAR★METHODS

Detailed methods are provided in the online version of this paper and include the following:

- KEY RESOURCES TABLE
- EXPERIMENTAL MODEL AND STUDY PARTICIPANT DETAILS
  - Cell lines and viruses
  - Alpaca
  - Mice
  - Study participants
- METHOD DETAILS
  - Protein purification
  - SEC-MALS analysis
  - Alpaca immunization, library construction and phage display
  - Production of VHHs and IgG-VHHs
  - Crystallization and structure determination
  - Cryo-electron microscopy
  - Bio-Layer Interferometry (BLI) measurements
  - Serpin activity assay
  - ELISA cross-competition assay
  - Generation of recombinant VACV
  - VACV MV and EV production
  - MV 24-hr yield, plaque assay and particle/PFU ratio
  - Early gene expression determination by qRT-PCR
  - Virus induced cell-cell fusion (fusion from without assay)
  - MPXV neutralization assay
  - VACV neutralization assay
  - Adsorption inhibition assay
  - Comet inhibition assay
  - Analysis of VACV virus yields by plaque assay
  - RNA isolation and quantification of VACV by reverse transcription-quantitative polymerase chain reaction (RT-qPCR)
  - Molecular dynamic simulations
  - In vivo evaluation in mice of the protective efficacy of the A56/K2-C05-Fc antibody against VACV
  - Mice immunization with rA16/G9 and evaluation of the protective efficacy against VACV
  - Serology studies (ELISA)

SUPPLEMENTAL INFORMATION

Supplemental information can be found online at https://doi.org/10.1016/j.cell.2025.07.040.

Received: January 30, 2025
Revised: June 10, 2025
Accepted: July 25, 2025

REFERENCES

1. Reardon, S. (2024). Mpox is spreading rapidly. Here are the questions researchers are racing to answer. Nature *633*, 16–17. https://doi.org/10.1038/d41586-024-02793-9.
2. Selverian, C.N., Monticelli, S.R., Jaleta, Y.M., Lasso, G., DeMouth, M.E., Meola, A., Berrigan, J., Batchelor, T.G., Battini, L., Guardado-Calvo, P., et al. (2024). MPXV Infection Stimulates a More Robust and Durable Neutralizing Antibody Response Compared to MVA-BN Vaccination. J. Infect. Dis *231*, 1069–1073. https://doi.org/10.1093/infdis/jiae515.
3. Postal, J., Guivel-Benhassine, F., Porrot, F., Grassin, Q., Crook, J.M., Vernuccio, R., Caro, V., Vanhomwegen, J., Guardado-Calvo, P., Simon-Lorière, E., et al. (2025). Antiviral activity of tecovirimat against monkeypox virus clades 1a, 1b, 2a, and 2b. Lancet Infect. Dis. *25*, e126–e127. https://doi.org/10.1016/S1473-3099(25)00014-3.
4. Vernuccio, R., Martínez León, A., Poojari, C.S., Buchrieser, J., Selverian, C.N., Jaleta, Y., Meola, A., Guivel-Benhassine, F., Porrot, F., Haouz, A., et al. (2025). Structural insights into tecovirimat antiviral activity and poxvirus resistance. Nat. Microbiol. *10*, 734–748. https://doi.org/10.1038/s41564-025-01936-6.
5. Smith, T.G., Gigante, C.M., Wynn, N.T., Matheny, A., Davidson, W., Yang, Y., Condori, R.E., O'Connell, K., Kovar, L., Williams, T.L., et al. (2023). Tecovirimat Resistance in Mpox Patients, United States, 2022–2023. Emerg. Infect. Dis. *29*, 2426–2432. https://doi.org/10.3201/eid2912.231146.
6. Lenharo, M. (2024). Hopes dashed for drug aimed at monkeypox virus spreading in Africa. Nature *632*, 965. https://doi.org/10.1038/d41586-024-02694-x.
7. Moss, B. (2016). Membrane fusion during poxvirus entry. Semin. Cell Dev. Biol. *60*, 89–96. https://doi.org/10.1016/j.semcdb.2016.07.015.
8. Gray, R.D.M., Albrecht, D., Beerli, C., Huttunen, M., Cohen, G.H., White, I.J., Burden, J.J., Henriques, R., and Mercer, J. (2019). Nanoscale polarization of the entry fusion complex of vaccinia virus drives efficient fusion. Nat. Microbiol. *4*, 1636–1644. https://doi.org/10.1038/s41564-019-0488-4.
9. Nelson, G.E., Wagenaar, T.R., and Moss, B. (2008). A conserved sequence within the H2 subunit of the vaccinia virus entry/fusion complex is important for interaction with the A28 subunit and infectivity. J. Virol. *82*, 6244–6250. https://doi.org/10.1128/JVI.00434-08.
10. Wagenaar, T.R., Ojeda, S., and Moss, B. (2008). Vaccinia virus A56/K2 fusion regulatory protein interacts with the A16 and G9 subunits of the entry fusion complex. J. Virol. *82*, 5153–5160. https://doi.org/10.1128/JVI.00162-08.
11. Wolfe, C.L., and Moss, B. (2011). Interaction between the G3 and L5 proteins of the vaccinia virus entry-fusion complex. Virology *412*, 278–283. https://doi.org/10.1016/j.virol.2011.01.014.
12. Hong, G.C., Tsai, C.H., and Chang, W. (2020). Experimental Evolution To Isolate Vaccinia Virus Adaptive G9 Mutants That Overcome Membrane Fusion Inhibition via the Vaccinia Virus A56/K2 Protein Complex. J. Virol. *94*, e00093-20. https://doi.org/10.1128/JVI.00093-20.
13. Cotter, C.A., and Moss, B. (2020). Mutations Near the N Terminus of Vaccinia Virus G9 Protein Overcome Restrictions on Cell Entry and Syncytium Formation Imposed by the A56/K2 Fusion Regulatory Complex. J. Virol. *94*, e00077-20. https://doi.org/10.1128/JVI.00077-20.
14. Mittler, E., Serris, A., Esterman, E.S., Florez, C., Polanco, L.C., O'Brien, C.M., Slough, M.M., Tynell, J., Gröning, R., Sun, Y., et al. (2023). Structural and mechanistic basis of neutralization by a pan-hantavirus protective antibody. Sci. Transl. Med. *15*, eadg1855. https://doi.org/10.1126/scitranslmed.adg1855.
15. Planchais, C., Fernández, I., Bruel, T., de Melo, G.D., Prot, M., Beretta, M., Guardado-Calvo, P., Dufloo, J., Molinos-Albert, L.M., Backovic, M., et al. (2022). Potent human broadly SARS-CoV-2-neutralizing IgA and IgG antibodies effective against Omicron BA.1 and BA.2. J. Exp. Med. *219*, e20220638. https://doi.org/10.1084/jem.20220638.
16. Mishra, A.K., Hellert, J., Freitas, N., Guardado-Calvo, P., Haouz, A., Fels, J.M., Maurer, D.P., Abelson, D.M., Bornholdt, Z.A., Walker, L.M., et al. (2022). Structural basis of synergistic neutralization of Crimean-Congo hemorrhagic fever virus by human antibodies. Science *375*, 104–109. https://doi.org/10.1126/science.abl6502.
17. Rouvinski, A., Guardado-Calvo, P., Barba-Spaeth, G., Duquerroy, S., Vaney, M.C., Kikuti, C.M., Navarro Sanchez, M.E., Dejnirattisai, W., Wongwiwat, W., Haouz, A., et al. (2015). Recognition determinants of broadly neutralizing human antibodies against dengue viruses. Nature *520*, 109–113. https://doi.org/10.1038/nature14130.
18. Kaever, T., Meng, X., Matho, M.H., Schlossman, A., Li, S., Sela-Culang, I., Ofran, Y., Buller, M., Crump, R.W., Parker, S., et al. (2014). Potent neutralization of vaccinia virus by divergent murine antibodies targeting a common site of vulnerability in L1 protein. J. Virol. *88*, 11339–11355. https://doi.org/10.1128/JVI.01491-14.
19. Su, H.P., Golden, J.W., Gittis, A.G., Hooper, J.W., and Garboczi, D.N. (2007). Structural basis for the binding of the neutralizing antibody, 7D11, to the poxvirus L1 protein. Virology *368*, 331–341. https://doi.org/10.1016/j.virol.2007.06.042.
20. Riccardo, V., and Pablo, G.C. (2023). Neutralization Determinants on Poxviruses. Viruses *15*, 2396. https://doi.org/10.3390/v15122396.
21. Hamers-Casterman, C., Atarhouch, T., Muyldermans, S., Robinson, G., Hamers, C., Songa, E.B., Bendahman, N., and Hamers, R. (1993). Naturally occurring antibodies devoid of light chains. Nature *363*, 446–448. https://doi.org/10.1038/363446a0.
22. DeHaven, B.C., Gupta, K., and Isaacs, S.N. (2011). The vaccinia virus A56 protein: a multifunctional transmembrane glycoprotein that anchors two secreted viral proteins. J. Gen. Virol. *92*, 1971–1980. https://doi.org/10.1099/vir.0.030460-0.
23. Zhou, A., Huntington, J.A., Pannu, N.S., Carrell, R.W., and Read, R.J. (2003). How vitronectin binds PAI-1 to modulate fibrinolysis and cell migration. Nat. Struct. Biol. *10*, 541–544. https://doi.org/10.1038/nsb943.
24. Chiu, H.-J., Wang, H.-C., and Chang, W. (2025). Structural Dissection of Vaccinia G9 Identifies Residues Essential for Membrane Fusion and Complex Assembly. Preprint at bioRxiv, 2025.2004.2022.650039. https://doi.org/10.1101/2025.04.22.650039.
25. Turner, P.C., and Moyer, R.W. (1995). Orthopoxvirus fusion inhibitor glycoprotein SPI-3 (open reading frame K2L) contains motifs characteristic of serine proteinase inhibitors that are not required for control of cell fusion. J. Virol. *69*, 5978–5987. https://doi.org/10.1128/JVI.69.10.5978-5987.1995.
26. Abramson, J., Adler, J., Dunger, J., Evans, R., Green, T., Pritzel, A., Ronneberger, O., Willmore, L., Ballard, A.J., Bambrick, J., et al. (2024). Accurate structure prediction of biomolecular interactions with AlphaFold 3. Nature *630*, 493–500. https://doi.org/10.1038/s41586-024-07487-w.
27. Priyamvada, L., Kallemeijn, W.W., Faronato, M., Wilkins, K., Goldsmith, C.S., Cotter, C.A., Ojeda, S., Solari, R., Moss, B., Tate, E.W., et al. (2022). Inhibition of vaccinia virus L1 N-myristoylation by the host N-myristoyltransferase inhibitor IMP-1088 generates non-infectious virions defective in cell entry. PLoS Pathog. *18*, e1010662. https://doi.org/10.1371/journal.ppat.1010662.

28. Girgis, N.M., Dehaven, B.C., Xiao, Y., Alexander, E., Viner, K.M., and Isaacs, S.N. (2011). The Vaccinia virus complement control protein modulates adaptive immune responses during infection. J. Virol. *85*, 2547–2556. https://doi.org/10.1128/JVI.01474-10.

29. Likos, A.M., Sammons, S.A., Olson, V.A., Frace, A.M., Li, Y., Olsen-Rasmussen, M., Davidson, W., Galloway, R., Khristova, M.L., Reynolds, M.G., et al. (2005). A tale of two clades: monkeypox viruses. J. Gen. Virol. *86*, 2661–2672. https://doi.org/10.1099/vir.0.81215-0.

30. Schmidt, F.I., Kuhn, P., Robinson, T., Mercer, J., and Dittrich, P.S. (2013). Single-virus fusion experiments reveal proton influx into vaccinia virions and hemifusion lag times. Biophys. J. *105*, 420–431. https://doi.org/10.1016/j.bpj.2013.06.016.

31. Gilchuk, I., Gilchuk, P., Sapparapu, G., Lampley, R., Singh, V., Kose, N., Blum, D.L., Hughes, L.J., Satheshkumar, P.S., Townsend, M.B., et al. (2016). Cross-Neutralizing and Protective Human Antibody Specificities to Poxvirus Infections. Cell *167*, 684–694.e9. https://doi.org/10.1016/j.cell.2016.09.049.

32. Misson Mindrebo, L., Liu, H., Ozorowski, G., Tran, Q., Woehl, J., Khalek, I., Smith, J.M., Barman, S., Zhao, F., Keating, C., et al. (2023). Fully synthetic platform to rapidly generate tetravalent bispecific nanobody-based immunoglobulins. Proc. Natl. Acad. Sci. USA *120*, e2216612120. https://doi.org/10.1073/pnas.2216612120.

33. Vigant, F., Santos, N.C., and Lee, B. (2015). Broad-spectrum antivirals against viral fusion. Nat. Rev. Microbiol. *13*, 426–437. https://doi.org/10.1038/nrmicro3475.

34. Kao, S., Kao, C.F., Chang, W., and Ku, C. (2023). Widespread Distribution and Evolution of Poxviral Entry-Fusion Complex Proteins in Giant Viruses. Microbiol. Spectr. *11*, e0494422. https://doi.org/10.1128/spectrum.04944-22.

35. Chang, H.W., Yang, C.H., Luo, Y.C., Su, B.G., Cheng, H.Y., Tung, S.Y., Carillo, K.J.D., Liao, Y.T., Tzou, D.M., Wang, H.C., et al. (2019). Vaccinia viral A26 protein is a fusion suppressor of mature virus and triggers membrane fusion through conformational change at low pH. PLOS Pathog. *15*, e1007826. https://doi.org/10.1371/journal.ppat.1007826.

36. Pokorny, L., Burden, J.J., Albrecht, D., Bamford, R., Leigh, K.E., Sridhar, P., Knowles, T.J., Modis, Y., and Mercer, J. (2024). The vaccinia chondroitin sulfate binding protein drives host membrane curvature to facilitate fusion. EMBO Rep. *25*, 1310–1325. https://doi.org/10.1038/s44319-023-00040-2.

37. Poojari, C.S., Bommer, T., and Hub, J.S. (2025). Viral fusion proteins of classes II and III recognize and reorganize complex biological membranes. Commun. Biol. *8*, 717. https://doi.org/10.1038/s42003-025-08040-9.

38. Aeffner, S., Reusch, T., Weinhausen, B., and Salditt, T. (2012). Energetics of stalk intermediates in membrane fusion are controlled by lipid composition. Proc. Natl. Acad. Sci. USA *109*, E1609–E1618. https://doi.org/10.1073/pnas.1119442109.

39. Danieli, T., Pelletier, S.L., Henis, Y.I., and White, J.M. (1996). Membrane fusion mediated by the influenza virus hemagglutinin requires the concerted action of at least three hemagglutinin trimers. J. Cell Biol. *133*, 559–569. https://doi.org/10.1083/jcb.133.3.559.

40. Pool, C.T., and Thompson, T.E. (1998). Chain length and temperature dependence of the reversible association of model acylated proteins with lipid bilayers. Biochemistry *37*, 10246–10255. https://doi.org/10.1021/bi980385m.

41. Yu, H., Resch, W., and Moss, B. (2025). Poxvirus structural biology for application to vaccine design. Trends Immunol. *46*, 455–470. https://doi.org/10.1016/j.it.2025.04.002.

42. Li, E., Yang, Q., Xie, W., Gong, Q., Guo, X., Zhou, J., Zhang, J., Chuai, X., Wang, Y., and Chiu, S. (2025). An mpox quadrivalent mRNA vaccine elicits sustained and protective immunity in mice against lethal vaccinia virus challenge. Emerg. Microbes Infect. *14*, 2447619. https://doi.org/10.1080/22221751.2024.2447619.

43. Ye, Q., Zhang, D., Zhang, R.R., Xu, Q., Huang, X.Y., Huang, B., Sun, M.X., Cong, Z., Zhu, L., Ma, J., et al. (2024). A penta-component mpox mRNA vaccine induces protective immunity in nonhuman primates. Nat. Commun. *15*, 10611. https://doi.org/10.1038/s41467-024-54909-4.

44. Kong, T., Du, P., Ma, R., Wang, H., Ma, X., Lu, J., Gao, Z., Qi, H., Li, R., Zhang, H., et al. (2024). Single-chain A35R-M1R-B6R trivalent mRNA vaccines protect mice against both mpox virus and vaccinia virus. EBiomedicine *109*, 105392. https://doi.org/10.1016/j.ebiom.2024.105392.

45. Ye, T., Zhou, J., Guo, C., Zhang, K., Wang, Y., Liu, Y., Zhou, J., Xie, Y., Li, E., Gong, R., et al. (2024). Polyvalent mpox mRNA vaccines elicit robust immune responses and confer potent protection against vaccinia virus. Cell Rep. *43*, 114269. https://doi.org/10.1016/j.celrep.2024.114269.

46. Zuiani, A., Dulberger, C.L., De Silva, N.S., Marquette, M., Lu, Y.J., Palowitch, G.M., Dokic, A., Sanchez-Velazquez, R., Schlatterer, K., Sarkar, S., et al. (2024). A multivalent mRNA monkeypox virus vaccine (BNT166) protects mice and macaques from orthopoxvirus disease. Cell *187*, 1363–1373.e12. https://doi.org/10.1016/j.cell.2024.01.017.

47. Freyn, A.W., Atyeo, C., Earl, P.L., Americo, J.L., Chuang, G.Y., Natarajan, H., Frey, T.R., Gall, J.G., Moliva, J.I., Hunegnaw, R., et al. (2023). An mpox virus mRNA-lipid nanoparticle vaccine confers protection against lethal orthopoxviral challenge. Sci. Transl. Med. *15*, eadg3540. https://doi.org/10.1126/scitranslmed.adg3540.

48. Liszewski, M.K., Bertram, P., Leung, M.K., Hauhart, R., Zhang, L., and Atkinson, J.P. (2008). Smallpox inhibitor of complement enzymes (SPICE): regulation of complement activation on cells and mechanism of its cellular attachment. J. Immunol. *181*, 4199–4207. https://doi.org/10.4049/jimmunol.181.6.4199.

49. Isaacs, S.N., Kotwal, G.J., and Moss, B. (1992). Vaccinia virus complement-control protein prevents antibody-dependent complement-enhanced neutralization of infectivity and contributes to virulence. Proc. Natl. Acad. Sci. USA *89*, 628–632. https://doi.org/10.1073/pnas.89.2.628.

50. Kotwal, G.J., Isaacs, S.N., McKenzie, R., Frank, M.M., and Moss, B. (1990). Inhibition of the complement cascade by the major secretory protein of vaccinia virus. Science *250*, 827–830. https://doi.org/10.1126/science.2237434.

51. Yu, H., Resch, W., Cotter, C.A., Xiao, W., Karamanolis, T., Belghith, A.A., Ignacio, M.A., Earl, P.L., Cohen, G.H., and Moss, B. (2025). Antibody Binding and Neutralizing Targets within the Predicted Structure of the Poxvirus Multiprotein Entry-Fusion Complex. Preprint at bioRxiv, 2025.05.07.652617. https://doi.org/10.1101/2025.05.07.652617.

52. Pütz, M.M., Midgley, C.M., Law, M., and Smith, G.L. (2006). Quantification of antibody responses against multiple antigens of the two infectious forms of Vaccinia virus provides a benchmark for smallpox vaccination. Nat. Med. *12*, 1310–1315. https://doi.org/10.1038/nm1457.

53. Kitchen, C.M., Nuño, M., Kitchen, S.G., and Krogstad, P. (2008). Enfuvirtide antiretroviral therapy in HIV-1 infection. Ther. Clin. Risk Manag. *4*, 433–439. https://doi.org/10.2147/tcrm.s1962.

54. Matho, M.H., Maybeno, M., Benhnia, M.R., Becker, D., Meng, X., Xiang, Y., Crotty, S., Peters, B., and Zajonc, D.M. (2012). Structural and biochemical characterization of the vaccinia virus envelope protein D8 and its recognition by the antibody LA5. J. Virol. *86*, 8050–8058. https://doi.org/10.1128/JVI.00836-12.

55. Matho, M.H., Schlossman, A., Meng, X., Benhnia, M.R., Kaever, T., Buller, M., Doronin, K., Parker, S., Peters, B., Crotty, S., et al. (2015). Structural and Functional Characterization of Anti-A33 Antibodies Reveal a Potent Cross-Species Orthopoxviruses Neutralizer. PLoS Pathog *11*, e1005148. https://doi.org/10.1371/journal.ppat.1005148.

56. Balière, C., Hourdel, V., Kwasiborski, A., Grassin, Q., Feher, M., Hoinard, D., Vanhomwegen, J., Taieb, F., Consigny, P.-H., Manuguerra, J.-C., et al. (2023). Complete Genome Sequences of Monkeypox Virus from a French Clinical Sample and the Corresponding Isolated Strain, Obtained Using Nanopore Sequencing. Microbiol. Resour. Announc. *12*, e0000923. https://doi.org/10.1128/mra.00009-23.

57. Batéjat, C., Grassin, Q., Feher, M., Hoinard, D., Vanhomwegen, J., Manuguerra, J.-C., and Leclercq, I. (2022). Heat inactivation of monkeypox virus. J. Biosaf. Biosecur. *4*, 121–123. https://doi.org/10.1016/j.jobb.2022.08.001.

58. Mercer, J., and Helenius, A. (2008). Vaccinia virus uses macropinocytosis and apoptotic mimicry to enter host cells. Science *320*, 531–535. https://doi.org/10.1126/science.1155164.

59. Yang, F., Lin, S., Chen, Z., Yue, D., Yang, M., He, B., Cao, Y., Dong, H., Li, J., Zhao, Q., et al. (2023). Structural basis of poxvirus A16/G9 binding for sub-complex formation. Emerg. Microbes Infect. *12*, 2179351. https://doi.org/10.1080/22221751.2023.2179351.

60. Robert, X., and Gouet, P. (2014). Deciphering key features in protein structures with the new ENDscript server. Nucleic Acids Res. *42*, W320–W324. https://doi.org/10.1093/nar/gku316.

61. Afonine, P.V., Grosse-Kunstleve, R.W., Echols, N., Headd, J.J., Moriarty, N.W., Mustyakimov, M., Terwilliger, T.C., Urzhumtsev, A., Zwart, P.H., and Adams, P.D. (2012). Towards automated crystallographic structure refinement with phenix.refine. Acta Crystallogr. D Biol. Crystallogr. *68*, 352–367. https://doi.org/10.1107/S0907444912001308.

62. McCoy, A.J., Grosse-Kunstleve, R.W., Adams, P.D., Winn, M.D., Storoni, L.C., and Read, R.J. (2007). Phaser crystallographic software. J. Appl. Crystallogr. *40*, 658–674. https://doi.org/10.1107/S0021889807021206.

63. Emsley, P., Lohkamp, B., Scott, W.G., and Cowtan, K. (2010). Features and development of Coot. Acta Crystallogr. D Biol. Crystallogr. *66*, 486–501. https://doi.org/10.1107/S0907444910007493.

64. Punjani, A., Rubinstein, J.L., Fleet, D.J., and Brubaker, M.A. (2017). cryoSPARC: algorithms for rapid unsupervised cryo-EM structure determination. Nat. Methods *14*, 290–296. https://doi.org/10.1038/nmeth.4169.

65. Goddard, T.D., Huang, C.C., and Ferrin, T.E. (2007). Visualizing density maps with UCSF Chimera. J. Struct. Biol. *157*, 281–287. https://doi.org/10.1016/j.jsb.2006.06.010.

66. Sanchez-Garcia, R., Gomez-Blanco, J., Cuervo, A., Carazo, J.M., Sorzano, C.O.S., and Vargas, J. (2021). DeepEMhancer: a deep learning solution for cryo-EM volume post-processing. Commun. Biol. *4*, 874. https://doi.org/10.1038/s42003-021-02399-1.

67. Morin, A., Eisenbraun, B., Key, J., Sanschagrin, P.C., Timony, M.A., Ottaviano, M., and Sliz, P. (2013). Collaboration gets the most out of software. eLife *2*, e01456. https://doi.org/10.7554/eLife.01456.

68. Jumper, J., Evans, R., Pritzel, A., Green, T., Figurnov, M., Ronneberger, O., Tunyasuvunakool, K., Bates, R., Žídek, A., Potapenko, A., et al. (2021). Highly accurate protein structure prediction with AlphaFold. Nature *596*, 583–589. https://doi.org/10.1038/s41586-021-03819-2.

69. Martínez-León, A. (2023). ale94mleon/TOFF: 0.1.0 . Zenodo https://doi.org/10.5281/zenodo.8189649.

70. Abraham, M.J., Murtola, T., Schulz, R., Páll, S., Smith, J.C., Hess, B., and Lindahl, E. (2015). GROMACS: High performance molecular simulations through multi-level parallelism from laptops to supercomputers. SoftwareX *1–2*, 19–25. https://doi.org/10.1016/j.softx.2015.06.001.

71. Hess, B., Bekker, H., Berendsen, H.J.C., and Fraaije, J.G.E.M. (1997). LINCS: A linear constraint solver for molecular simulations. J. Comp. Chem. *18*, 1463–1472. https://doi.org/10.1002/(SICI)1096-987X(199709)18:12<1463::AID-JCC4>3.0.CO;2-H.

72. Krissinel, E., and Henrick, K. (2004). Secondary-structure matching (SSM), a new tool for fast protein structure alignment in three dimensions. Acta. Crystallogr. D. Biol. Crystallogr. *60*, 2256–2268. https://doi.org/10.1107/S0907444904026460.

73. Tsai, Y.X., Chang, N.E., Reuter, K., Chang, H.T., Yang, T.J., von Bülow, S., Sehrawat, V., Zerrouki, N., Tuffery, M., Gecht, M., et al. (2024). Rapid simulation of glycoprotein structures by grafting and steric exclusion of glycan conformer libraries. Cell *187*, 1296–1311.e26. https://doi.org/10.1016/j.cell.2024.01.034.

74. Kabsch, W. (2010). Integration, scaling, space-group assignment and post-refinement. Acta Crystallogr. D Biol. Crystallogr. *66*, 133–144. https://doi.org/10.1107/S0907444909047374.

75. Hubert, M., Guivel-Benhassine, F., Bruel, T., Porrot, F., Planas, D., Vanhomwegen, J., Wiedemann, A., Burrel, S., Marot, S., Palich, R., et al. (2023). Complement-dependent mpox-virus-neutralizing antibodies in infected and vaccinated individuals. Cell Host Microbe *31*, 937–948.e4. https://doi.org/10.1016/j.chom.2023.05.001.

76. Treutiger, C.J., Filén, F., Rehn, M., Aarum, J., Jacks, A., Gisslén, M., Sturegård, E., Karlberg, M.L., Karlsson Lindsjö, O., and Sondén, K. (2024). First case of mpox with monkeypox virus clade Ib outside Africa in a returning traveller, Sweden, August 2024: public health measures. Euro Surveill. *29*, 2400740. https://doi.org/10.2807/1560-7917.ES.2024.29.48.2400740.

77. Backovic, M., Johansson, D.X., Klupp, B.G., Mettenleiter, T.C., Persson, M.A.A., and Rey, F.A. (2010). Efficient method for production of high yields of Fab fragments in Drosophila S2 cells. Protein Eng. Des. Sel. *23*, 169–174. https://doi.org/10.1093/protein/gzp088.

78. Meola, A., and Guardado-Calvo, P. (2024). Production and Purification of Hantavirus Glycoproteins in Drosophila melanogaster S2 Cells. Methods Mol. Biol. *2762*, 3–16. https://doi.org/10.1007/978-1-0716-3666-4_1.

79. Gransagne, M., Aymé, G., Brier, S., Chauveau-Le Friec, G., Meriaux, V., Nowakowski, M., Dejardin, F., Levallois, S., Dias de Melo, G., Donati, F., et al. (2022). Development of a highly specific and sensitive VHH-based sandwich immunoassay for the detection of the SARS-CoV-2 nucleoprotein. J. Biol. Chem. *298*, 101290. https://doi.org/10.1016/j.jbc.2021.101290.

80. Moeglin, E., Desplancq, D., Stoessel, A., Massute, C., Ranniger, J., McEwen, A.G., Zeder-Lutz, G., Oulad-Abdelghani, M., Chiper, M., Lafaye, P., et al. (2021). A Novel Nanobody Precisely Visualizes Phosphorylated Histone H2AX in Living Cancer Cells under Drug-Induced Replication Stress. Cancers (Basel) *13*, 3317. https://doi.org/10.3390/cancers13133317.

81. Weber, P., Pissis, C., Navaza, R., Mechaly, A.E., Saul, F., Alzari, P.M., and Haouz, A. (2019). High-Throughput Crystallization Pipeline at the Crystallography Core Facility of the Institut Pasteur. Molecules *24*, 4451. https://doi.org/10.3390/molecules24244451.

82. Agirre, J., Atanasova, M., Bagdonas, H., Ballard, C.B., Baslé, A., Beilsten-Edmands, J., Borges, R.J., Brown, D.G., Burgos-Mármol, J.J., Berrisford, J.M., et al. (2023). The CCP4 suite: integrative software for macromolecular crystallography. Acta Crystallogr. D Struct. Biol. *79*, 449–461. https://doi.org/10.1107/S2059798323003595.

83. Williams, C.J., Headd, J.J., Moriarty, N.W., Prisant, M.G., Videau, L.L., Deis, L.N., Verma, V., Keedy, D.A., Hintze, B.J., Chen, V.B., et al. (2018). MolProbity: More and better reference data for improved all-atom structure validation. Protein Sci. *27*, 293–315. https://doi.org/10.1002/pro.3330.

84. Afonine, P.V., Klaholz, B.P., Moriarty, N.W., Poon, B.K., Sobolev, O.V., Terwilliger, T.C., Adams, P.D., and Urzhumtsev, A. (2018). New tools for the analysis and validation of cryo-EM maps and atomic models. Acta Crystallogr. D Struct. Biol. *74*, 814–840. https://doi.org/10.1107/S2059798318009324.

85. Jensen, J.K., Thompson, L.C., Bucci, J.C., Nissen, P., Gettins, P.G.W., Peterson, C.B., Andreasen, P.A., and Morth, J.P. (2011). Crystal structure of plasminogen activator inhibitor-1 in an active conformation with normal thermodynamic stability. J. Biol. Chem. *286*, 29709–29717. https://doi.org/10.1074/jbc.M111.236554.

86. Zhao, R., Wu, L., Sun, J., Liu, D., Han, P., Gao, Y., Zhang, Y., Xu, Y., Qu, X., Wang, H., et al. (2024). Two noncompeting human neutralizing antibodies targeting MPXV B6 show protective effects against orthopoxvirus infections. Nat. Commun. *15*, 4660. https://doi.org/10.1038/s41467-024-48312-2.

87. Pachitariu, M., Rariden, M., and Stringer, C. (2025). Cellpose-SAM: superhuman generalization for cellular segmentation. Preprint at bioRxiv, 2025.04.28.651001. https://doi.org/10.1101/2025.04.28.651001.

88. Stringer, C., Wang, T., Michaelos, M., and Pachitariu, M. (2021). Cellpose: a generalist algorithm for cellular segmentation. Nat. Methods *18*, 100–106. https://doi.org/10.1038/s41592-020-01018-x.

89. van der Walt, S., Schönberger, J.L., Nunez-Iglesias, J., Boulogne, F., Warner, J.D., Yager, N., Gouillart, E., and Yu, T.; scikit-image contributors (2014). scikit-image: image processing in Python. PeerJ *2*, e453. https://doi.org/10.7717/peerj.453.

90. Fedele, C.G., Negredo, A., Molero, F., Sánchez-Seco, M.P., and Tenorio, A. (2006). Use of internally controlled real-time genome amplification for detection of variola virus and other orthopoxviruses infecting humans. J. Clin. Microbiol. *44*, 4464–4470. https://doi.org/10.1128/JCM.00276-06.

91. Maier, J.A., Martinez, C., Kasavajhala, K., Wickstrom, L., Hauser, K.E., and Simmerling, C. (2015). ff14SB: Improving the Accuracy of Protein Side Chain and Backbone Parameters from ff99SB. J. Chem. Theor. Comput. *11*, 3696–3713. https://doi.org/10.1021/acs.jctc.5b00255.

92. Wang, J., Wolf, R.M., Caldwell, J.W., Kollman, P.A., and Case, D.A. (2004). Development and testing of a general amber force field. J. Comput. Chem. *25*, 1157–1174. https://doi.org/10.1002/jcc.20035.

93. Jorgensen, W.L., Chandrasekhar, J., Madura, J.D., Impey, R.W., and Klein, M.L. (1983). Comparison of simple potential functions for simulating liquid water. J. Chem. Phys. *79*, 926–935. https://doi.org/10.1063/1.445869.

94. Bussi, G., Donadio, D., and Parrinello, M. (2007). Canonical sampling through velocity rescaling. J. Chem. Phys. *126*, 014101. https://doi.org/10.1063/1.2408420.

95. Bernetti, M., and Bussi, G. (2020). Pressure control using stochastic cell rescaling. J. Chem. Phys. *153*, 114107. https://doi.org/10.1063/5.0020514.

96. Darden, T., York, D., and Pedersen, L. (1993). Particle mesh Ewald: An N·log(N) method for Ewald sums in large systems. J. Chem. Phys. *98*, 10089–10092. https://doi.org/10.1063/1.464397.

97. Essmann, U., Perera, L., Berkowitz, M.L., Darden, T., Lee, H., and Pedersen, L.G. (1995). A smooth particle mesh Ewald method. J. Chem. Phys. *103*, 8577–8593. https://doi.org/10.1063/1.470117.

Please cite this article in press as: Meola et al., Structural basis of poxvirus fusion regulation and anti-A16/G9 antibody-mediated neutralization and protection, Cell (2025), https://doi.org/10.1016/j.cell.2025.07.040

STAR★METHODS

KEY RESOURCES TABLE

REAGENT or RESOURCE	SOURCE	IDENTIFIER
Antibodies		
Peroxidase Goat Anti-Human IgG (H+L)	Jackson ImmunoResearch	Cat# 109-035-088; RRID:AB_2337584
Goat anti-Human IgG	ThermoFisher	Cat# H17000; RRID:AB_1500566
Vaccinia Virus Polyclonal Antibody	Invitrogen	Cat# PA1-7258; RRID:AB_561894
AlexaFluor 488-coupled goat anti-rabbit antibody	Invitrogen	Cat# A.-11008; RRID:AB_143165
Anti-B5 monoclonal antibody VACV283	Gilchuk et al.[31]	N/A
Anti-A27 monoclonal antibody VACV302	Gilchuk et al.[31]	N/A
Anti-L1 monoclonal antibody 7D11	Schmidt et al.[30]	N/A
Anti-D8 monoclonal antibody LA5	Matho et al.[54]	N/A
Anti-A33 monoclonal antibody A20G2	Matho et al.[55]	N/A
Bacterial and virus strains		
BL21 (DE3) Competent E. Coli	New England BioLabs	Cat# C2527H
MPXV/2022/FR/CMIP	Cellule d'Intervention Biologique d'Urgence of Institut Pasteur, Paris, France	GISAID: EPI_ISL_16260402 Balière et al.[56] Batéjat et al.[57]
VACV strain Western Reserve (WR)-GFP	Mercer, Birmingham University	Mercer and Helenius[58]
VACV strain Western Reserve (WR)	Mercer, Birmingham University	Mercer and Helenius[58]
VACV strain Western Reserve (WR)_G9(G2A)	Mercer, Birmingham University	This paper
VACV strain Western Reserve (WR)_A16(G2A)	Mercer, Birmingham University	This paper
VACV strain Western Reserve (WR)_ G9(G2A):A16(G2A)	Mercer, Birmingham University	This paper
VACV strain IHD-J	Mercer, Birmingham University	Mercer and Helenius[58]
Biological samples		
Sera	Agence de la Biomédicine	PFS07-009
Sera	Henri Mondor University Hospital (AP-HP)	MEMO-COV-2 study (NCT04402892, CPP Ile-de-France VI); "Collection Vaccin" (2018-A01610-55, CPP EST-III)
Chemicals, peptides, and recombinant proteins		
LM-SFM4 Insect with L-Glutamine medium	Cytiva	Cat# SH30913.03
Expi293 expression medium	Gibco	Cat# 1435101
Puromycin	Invivogen	Cat# ant-pr-5
Thrombin	Cytiva	Cat# 27-0846-01
Isopropyl β-*d*-1-thiogalactopyranoside (IPTG)	Euromedex	Cat# EU0008-B
Protease Inhibitor Tablets, EDTA-free	Thermo Scientific	Cat# A32965
KPL SureBlue™ TMB Microwell Peroxidase substrate	Eurobio	Cat# 5120-0077
1-Step™ Ultra TMB substrate	Thermo Scientific	Cat# 34028
Urokinase-type plasminogen activator, uPA	Millipore	Cat# CC4000
Alexa Fluor 594-phalloidin	Invitrogen	A12381
Hoechst-33258	Invitrogen	H1398
Critical commercial assays		
Biotinylation Kit	Avidity LLC	Cat# BirA500
FectoPRO®	OZYME	Cat# POL10100000 7
iTaq™ Universal SYBR® Green Supermix	Biorad	Cat#1725124
DNeasy® Blood & Tissue Kit	QIAGEN	Cat#69504

(*Continued on next page*)

Please cite this article in press as: Meola et al., Structural basis of poxvirus fusion regulation and anti-A16/G9 antibody-mediated neutralization and protection, Cell (2025), https://doi.org/10.1016/j.cell.2025.07.040

Continued

REAGENT or RESOURCE	SOURCE	IDENTIFIER
Deposited data		
A16/G9/A56^{IG}/K2 at pH 8 Cryo-EM maps	This paper	EMDB: 52019
A16/G9/A56^{IG}/K2 at pH 5.5 Cryo-EM maps	This paper	EMDB: 53936
Atomic coordinate of A16/G9/A56^{IG}/K2 at pH 8	This paper	PDB: 9HBK
Atomic coordinates of A16/G9/A56^{IG}/K2 at pH 5.5	This paper	PDB: 9RDH
Atomic coordinates and structure factors for A56^{IG}/K2	This paper	PDB: 9HL2
Atomic coordinates and structure factors for A16/G9/D07/B01/C05	This paper	PDB: 9HLS
Atomic coordinates and structure factors for A16/G9/D07/E12	This paper	PDB: 9HPA
Atomic coordinates and structure factors for A16/G9^{H44Y}/D07	This paper	PDB: 9HNG
Atomic coordinates and structure factors for A16/G9/D07 at pH 5.7	This paper	PDB: 9R09
Atomic coordinates and structure factors for A16/G9/D07 at pH 6.5	This paper	PDB: 9R0B
Atomic coordinates and structure factors for A16/G9/D07 at pH 7.2	This paper	PDB: 9R0J
Atomic coordinates of A16/G9	Yang et al.[59]	PDB: 8GP6
Experimental models: Cell lines		
Drosophila S2 cells	ThermoFischer	Cat#R69007
Expi293F™ Cells	ThermoFisher	Cat#A14527
Vero E6	ATCC	Cat# CRL-1586; RRID: CVCL_YZ66
BSC40	ATTC	Cat# CRL-2761; RRID: CVCL_3656
U2OS	ATCC	Cat# HTB-96; RRID: CVCL_0042
HeLa	ATCC	Cat# CCL-2 RRID: CVCL_0030
Experimental models: Organisms/strains		
Mouse: Female C57BL/6	*Envigo* RMS LLC	RRID: MGI:2159769
Oligonucleotides		
Primer: C11R Forward: AAACACACACTGAGAAACAGCATAAA	This paper	N/A
Primer: C11R Reverse: ACTATCGGCGAATGATCTGATTA	This paper	N/A
Recombinant DNA		
pT350- A16/G9	GenScript	N/A
pCOPURO	Addgene	RRID:Addgene_17533
pT667-A56^{Ig}/K2	GenScript	N/A
pT667- A16/G9_H44Y	GenScript	N/A
pT667- A16/G9_Y42C	GenScript	N/A
pT667- A16_Y103R/G9	GenScript	N/A
pT667- A16_A17R/G9	GenScript	N/A
pCAGGS_ IgG1-VHH-E12	GenScript	N/A
pCAGGS_ IgG1-VHH-D07	GenScript	N/A
pCAGGS_ IgG1-VHH-B01	GenScript	N/A
pCAGGS_ IgG1-VHH-C05	GenScript	N/A
pT667_7D11	GenScript	N/A
pCAGGS_LA5_LC	GenScript	N/A
pCAGGS_LA5_HC	GenScript	N/A
pT667_VACV302	GenScript	N/A
pCAGGS_VACV283_HC	GenScript	N/A
pCAGGS_VACV283_LC(k)	GenScript	N/A

(*Continued on next page*)

Continued

REAGENT or RESOURCE	SOURCE	IDENTIFIER
pCAGGS_A56^{Ig}/K2_C05_Fc	GenScript	N/A
pET28c(+)_PAI-1-W175F	GenScript	N/A
pET28c(+)_K2	GenScript	N/A
pT350_qPCR_standard	GenScript	N/A
Software and algorithms		
Harmony High-Content Imaging and Analysis Software	PerkinElmer	Cat#HH17000012
GraphPad Prism 10 (Version 10.2.1)	Graphpad	https://www.graphpad.com
ESPript	Robert et al.[60]	https://espript.ibcp.fr
Phenix.refine	Afonine et al.[61]	https://www.phenix-online.org/
PHASER (version 2.8.3)	McCoy et al.[62]	https://phaser.io/download/release/v2.8.3
Coot	Emsley et al.[63]	https://www2.mrc-lmb.cam.ac.uk/personal/pemsley/coot/
CryoSPARC	Punjani et al.[64]	https://cryosparc.com
Chimera	Goddard et al.[65]	https://www.cgl.ucsf.edu/chimera/
DeepEMhancer	Sanchez-Garcia et al.[66]	https://github.com/rsanchezgarc/deepEMhancer
Pymol	Schrodinger, LLC	https://www.pymol.org
SBGrid	Morin et al.[67]	https://sbgrid.org
Alphafold2	Jumper et al.[68]	https://colab.research.google.com/github/sokrypton/ColabFold/blob/main/AlphaFold2.ipynb
Alphafold3	Abramson et al.[26]	https://alphafoldserver.com/welcome
TOFF	Martínez-León[69]	https://toff.readthedocs.io/en/latest/source/installation.html
Octet Analysis Studio (Version 13.0)	Sartorius	Sartorius
GROMACS-2022.4	Abraham et al.[70]	https://manual.gromacs.org/documentation/2022.4/download.html
LINCS algorithm	Hess et al.[71]	https://manual.gromacs.org/2024.4/reference-manual/algorithms/constraint-algorithms.html
FluoroSpot Software (Version 7.0.22.1)	InmunoSpot, CTL	https://immunospot.com/products/
Astra Software (Version 6.1.7)	Wyatt	https://www.wyatt.com/products/software/astra.html
PDBeFold	Krissinel and Henrick[72]	https://www.ebi.ac.uk/msd-srv/ssm/
GlycoSHIELD	Tsai et al.[73]	https://dioscuri-biophysics.pages.mpcdf.de/glycoshield-md/
XDS (version 10 January 2022)	Kabsch[74]	https://xds.mr.mpg.de
Other		
HiTrap TALON 5ml	Cytiva	Cat# 28953767
HiTrap Protein G HP	Cytiva	Cat# 17040501
Strep-Tactin® Superflow® high capacity	IBA	Cat# 2-1240-001
Superdex 75 Increase 10/300GL	Cytiva	Cat# 29148721
Superdex 200 Increase 10/300GL	Cytiva	Cat# 28990944
HiLoad 16/600 Superdex 200pg	Cytiva	Cat# 28989335
UltrAuFoil® Holey Gold Films – Geom. R 1.2/1.3 – on Gold 300mesh 50/B	Delta Microscopies	Cat# Q-UltrAuFoil-R1.2_1.3
Guinea Pig Serum	Rockland Inc.	Cat# D105-00-0050
Baby Rabbit Complement	Cedarlane Laboratories Limited	Cat# CL3441-S100-R
Octet® Streptavidin (SA) Biosensors	Sartorius	Cat# 18-5019
Octet® Anti-Penta-HIS (HIS1K) Biosensors	Sartorius	Cat# 18-5120
Octet® AHC Biosensors	Sartorius	Cat# 18-5060

Please cite this article in press as: Meola et al., Structural basis of poxvirus fusion regulation and anti-A16/G9 antibody-mediated neutralization and protection, Cell (2025), https://doi.org/10.1016/j.cell.2025.07.040

EXPERIMENTAL MODEL AND STUDY PARTICIPANT DETAILS

Cell lines and viruses

Drosophila S2 cells (primary culture of late-stage drosophila melanogaster embryos, Thermo Fisher Scientific) were grown at 28°C in serum-free LM-SFM4Insect cell medium (Cytiva). Expi293F™ cells (human embryonic kidney cells, Thermo Fisher Scientific) were grown at 37°C with 8% CO_2 and a constant shaking speed of 130 RPM in Expi293 Expression Medium (Thermo Fisher Scientific) and transfected in Expi293 FreeStyle Medium (Thermo Fisher Scientific). BSC-40 (Cercopithecus aethiops kidney epithelial cells, ATCC CRL-2761), HeLa (human female cervical cancer cells, ATCC CCL-2) and U2OS (human female osteosarcoma cells, ATCC HTB-96) cells were cultured in DMEM GlutaMAX (Gibco) supplemented with 10% heat-inactivated FBS (Cytiva), 100 U/mL penicillin and 100 U/mL streptomycin (Gibco) and maintained at 37°C with 5% CO_2.

The VACV Western Reserve strain (ATCC VR-119) encoding for GFP reporter gene and the IDH-J strain were obtained from the laboratory of Jason Mercer. The virus was handled under BSL-2 conditions by trained personnel. The MPXV clade IIb strain (MPXV/2022/FR/CMIP) was isolated from a pustular lesion of a 36-year-old French man who consulted at the Medical Center of Institut Pasteur (CMIP), in June 2022. The clinical specimen was inoculated on Vero E6 cells (ATTC CRL-1586), whose supernatant was harvested after 3 days and tested positive for the presence of MPXV by PCR.[57,75] The titration of viral stocks was performed on U2OS cells.[56,75] The 3rd cell passage of the virus was used. The MPXV clade Ib strain was isolated from a man in his mid-30s with no history of orthopoxvirus vaccination and traveling between Sweden and Africa in August 2024.[76] The isolate MpxV/PHAS-506/Passage- 03/SWE/2024_09_11, Clade Ib has been provided by the Public Health Agency of Sweden to improve the quality of diagnostics relevant for infectious disease control, treatment and/or other studies of relevance for public health. The 5th cell passage of the virus was used. All experiments with MPXV were conducted under BSL-3 conditions by vaccinated personnel according to the French regulations on dual use pathogens.

Alpaca

The alpaca used in this study (one young male adult) was housed in a llama/alpaca animal facility in Rennemoulin (France) (Agreement number A7832214). Animal procedures were conducted in accordance with French legislation and complied with the European Communities Council Directives (2010/63/UE, French Law 2013–118, February 6, 2013). This study was approved by the Animal Experimentation Ethics Committee of the Institut Pasteur (CETEA 89) (2020–27412).

Mice

Female C57BL/6 mice (12 weeks old) were obtained from EnVigo Laboratories and housed at the CNB-CSIC (Madrid, Spain) under specific-pathogen-free conditions. Experimental procedures were approved by the Ethical Committees of Animal Experimentation (CEEA) of the CNB-CSIC and CSIC, as well as by the Division of Animal Protection of the Comunidad de Madrid (PROEX 228.7/23) and complied with international ethical guidelines and Spanish law (Royal Decree RD 53/2013).

Study participants

Human sera used in Figure 7 were collected from 2 independent cohorts. First, sera were collected and analysed from organ donors and were obtained from the Agence de la Biomédecine (PFS07-009). Donors with lymphoma, autoimmune disease or positive serology for HIV, HCV or HBV were excluded. Second, sera were collected in the context of longitudinal follow-up of COVID-19 and Modified Vaccinia Ankara - Bavarian Nordic (MVA-BN) vaccinated patients or health-care workers recruited at the Henri Mondor University Hospital (AP-HP), between January 2021 and July 2024 (MEMO-COV-2 study (NCT04402892, CPP Ile-de-France VI) and (“Collection Vaccin” (2018-A01610-55, CPP EST-III)). This study was conducted in compliance with the Declaration of Helsinki principles and written informed consent was obtained from all participants.

While we did not have access to smallpox vaccination records from most donors in these two cohorts, we postulated that donors born before 1977 would likely have received at least one dose of the anti-smallpox vaccine (VACV) in accordance with recommended vaccinations at the time. Conversely, donors born after 1980, following the official eradication of smallpox, are unlikely to have been vaccinated and thus should not have circulating smallpox/VACV-specific antibodies. Information on age, sex, and relevant clinical features of the cohort are provided in Table S3. No sample size calculation, randomization, or blinding were performed for this study.

METHOD DETAILS

Protein purification

To obtain $A56^{IG}$/K2 and A16/G9 complexes, we inserted codon-optimized synthetic genes for expression in Drosophila S2 cells into a bicistronic plasmid.[77] All sequences were derived from the VACV Western Reserve (WR) strain and were cloned in frame with a signal peptide that targets them to the secretory pathway. The first cistron of pMT-$A56^{IG}$/K2 included the region 20–131 of A56 (UniProt code: Q01218), followed by a hexa-histidine tag. The second cistron contains the region 16–369 of K2 (UniProt code: P18384), in which we included the mutation C109A to avoid the formation of disulfide-bonded dimers. The first cistron of pMT-A16/G9 included the region 3–295 of A16 (P16710) followed by a hexa-histidine and an Avi tag, and the second cistron the region 3–271 of G9 (P07611) followed by a double strep-tag. To avoid unnatural glycosylation in A16/G9, we mutated the exposed N-glycosylation motifs by

introducing the mutations N82A, N93Q, S156A and N157D in G9. All other mutations mentioned in the text were created on these plasmids. To produce the ectodomains of A33 (UniProt code: P68617, residues 90–185), and B5 from VACV (Q01227, residues 18–279), we cloned them into a pMT/BiP plasmid suitable for expression in Drosophila melanogaster S2 cells in frame with a double-strep tag and an AviTag at the C-terminus.

To obtain stable transfectants of Drosophila S2 cells, each one of the described plasmid was co-transfected with pCoPuro plasmid (ratio 1:20) for puromycin selection.[78] Stable cell lines were selected and maintained in LM-SFM4 medium (Cytiva) containing 8 μg/mL puromycin. Cultures of 1–3 liters were grown in spinner flasks in medium supplemented with 1% penicillin/streptomycin antibiotics to approximately 1×10^7 cells/mL, and protein expression was induced with 4 μM $CdCl_2$. After 5 days, the S2 media supernatant was concentrated to 50 ml using 10 KDa cutoff VivaFlow concentrator (Sartorius) and supplemented with Biolock (IBA) and 0.1M Tris-HCl (pH 8.0), centrifuged for 30 min at 50,000 g. Proteins were purified on an AKTAgo instrument (Cytiva) by using affinity chromatography on StrepTactin SuperFlow column (IBA) followed by SEC on a HiLoad 16/600 Superdex75 column (Cytiva) in 10 mM Tris pH 8.0, 100 mM NaCl. The yields were approximately 7 mg/L for rA16/G9, 4 mg/L for $A56^{IG}$/K2 cells; 5 mg/L for A33 and 2 mg/L for B5 cells For binding experiments in Figure S2C, $A56^{IG}$ was deglycosilated by adding EndoD and EndoH in equimolar amount and incubating overnight at 4°C.

SEC-MALS analysis

SEC-MALS experiments were performed loading 100 μg of each protein into a Superdex200 10/300 column (Cytiva) at a flow rate of 0.4 ml/min, previously equilibrated with SEC buffer (10mM Tris pH 8, 150nM NaCl) (Figure 1) or the tri-component buffer (100mM Tris; 50mM MES, 50mM sodium acetate, 150mM NaCl). The complex $A56^{IG}$/K2/A16/G9 was obtained mixing $A56^{IG}$/K2 and rA16/G9 (2:1 mol/mol), overnight at 4°C. Online MALS detection was performed with a DAWN-HELEOS II detector (Wyatt Technology, Santa Barbara, CA, USA). Differential refractive index measurement was performed with an Optilab T-rEX detector (Wyatt Technology). Data were analyzed, and weight-averaged molecular masses (Mw) for each sample were calculated using the Astra software (Wyatt Technology).

Alpaca immunization, library construction and phage display

One young adult male alpaca (*Vicugna pacos*) received immunization on days 0, 17, and 24 with 150 μg of rA16/G9 previously digested with thrombin to remove the purification tags. The immunogen was mixed with Freund's complete adjuvant for the initial immunization and with Freund's incomplete adjuvant for subsequent immunizations. Immune response was monitored by titrating serum samples using ELISA with the coated antigen and polyclonal rabbit anti-alpaca IgG.

Blood was collected from the immunized animal (approximately 200 mL), and peripheral blood lymphocytes were isolated by centrifugation on a Ficoll discontinuous gradient (Leucosep Tubes, Greiner) and stored at -80°C until further use. Total RNA and cDNA were obtained as previously described,[79] and nested PCR was performed using IgG-specific primers.[80] In the first step, five sets of PCR primers were used to amplify VH-CH1-CH2 and VHH-CH2 fragments. Bands corresponding to the VHH-CH2 regions were purified by agarose gel electrophoresis. Next, the VHH regions were specifically reamplified with three sets of VHH-specific PCR primers complementary to the 5′ and 3′ ends of the amplified product and incorporating Sfi1 and Not1 restriction sites at the ends of the VHH genes. PCR products were digested and ligated into the pHEN6 phagemid vector.

Next, we used the phage display technology to select antigen-specific phage-VHHs. We used 1013 phage-VHHs to perform three rounds of panning in which phages-VHHs were incubated with strep-tagged rA16/G9 for 1 h at RT, and the complex was trapped using StrepTactin beads (Mag step XT beads, IBA)). 100 μM of strep-tagged rA16/G9 was used for the first round of panning; 10 μM and 1 μM of strep-tagged protein were used for the second and third rounds of panning, respectively. To remove nonspecific binders, six washes with PBS Tween 0.1% and four washes with PBS were performed, followed by elution with 100 mM triethylamine (TEA) for 5 min on a wheel, and excess TEA was neutralized immediately with 1 M Tris-HCl (pH 7.6). E. coli TG1 cells in the exponential growth phase were then infected with eluted phage-VHHs and incubated at 37 °C for 30 min without stirring and 30 min under stirring. The bacteria were spread on a 2YT+ampicillin Bio-assay dish (24 cm x24 cm) and incubated overnight at 30 °C.

Phage-VHHs were produced from individual colonies, and binding of the phages to the protein on the plate was revealed using an anti-M13 monoclonal antibody conjugated to peroxidase (Abcam). The VHH nucleotide sequences were determined using the M13-40 primer (Eurofins).

Production of VHHs and IgG-VHHs

To express monomeric VHHs in bacteria, we cloned codon-optimized sequences of the selected VHHs into the bacterial expression vector pET28c(+) (Novagen) with a C-terminal His tag. We transformed E. coli BL21 (DE3) cells (New England Biolabs) and induce protein expression overnight at 16°C with 0.5 mM isopropyl β-d-1-thiogalactopyranoside (IPTG). Cells harvested from 3 L of culture were resuspended in 40 mL cold resuspension buffer (PBS pH 7.4, 5 mM imidazole) supplemented by one tablet of EDTA-free complete protease inhibitor (Thermo Scientific A32965), frozen at -20° C and lysed using a sonicator. After removing the insoluble material by centrifugating at 50,000 g for 30 minutes, we purified the recombinant VHHs using TALON affinity columns followed by SEC with a Superdex 75 column (Cytiva). To express the bivalent VHH-Fc in mammalian cells, we inserted codon-optimized sequences into a mammalian expression vector pCAGGS (ENA code: LT727518.1) in frame with an human IgG1 Fc at the C-terminal end. To express antibodies, heavy (human IgG1) and light chains codon-optimized sequences were cloned into the pCAGGS vector. Proteins were expressed in Expi293 cells (Thermo Fischer), transfected at a density of $3x10^6$ cells/mL using FectroPRO DNA transfection reagent

(Polyplus). After 5 days incubation at 37° C, the supernatant was harvested and centrifuged (30 minutes, 4000 rpm). Antibodies were purified using protein G affinity chromatography, eluted using 0.1 M glycine pH 2.7 and neutralized with 1 M Tris-HCl pH 8.0. The eluate was concentrated and used to perform a SEC in PBS. The final yields were 7 mg/L for VHH-D07, 0.33 mg/L for VHH-C05, 0.25 mg/L for VHH-B01, 2 mg/L for VHH-E12, 13 mg/100 mL for IgG-VHH D07, 0.60 mg/100 mL for IgG-VHH C05, 15.30 mg/100 mL for IgG-VHH B01 and 10.50 mg/100 mL for IgG-VHH E12.

Crystallization and structure determination

For crystallization, purification tags were cleaved using 1.5 units of thrombin (Cytiva) per 0.1 mg of protein overnight at 4°C before SEC, and the monomeric peaks were concentrated in 10 mM Tris-HCl pH 8.0, 150 mM NaCl, using Vivaspin centricons, to a final concentration of 2–10 mg/mL. Crystallization screening trials were carried out by the vapor diffusion method using a Mosquito TM nanodispensing system (STPLabtech, Melbourn, UK) following established protocols.[81] The best crystals of A56^{IG}/K2 were grown in 0.2 M Na_3 citrate, 0.1 M Tris-HCl pH 8.5, 30% (v/v) PEG 400. Crystals of rA16/G9 in complex with VHH-D07 were grown in 0.1 M MES pH 5.5, 6.5, or 7.5 12% (w/v) PEG 20K and cryo protected in the same solution supplemented with 33% glycerol. Crystals of rA16/G9^{H44Y} in complex with VHH-D07 were grown in 20% (w/v) PEG 4K, 10% (v/v) glycerol, 0.2M $MgSO_4$ and cryo-protected in the same solution supplemented with 20% (v/v) glycerol. Crystals of rA16/G9 in complex with VHH-D07 and VHH-E12 were grown in 20% (w/v) PEG 1000, 0.1M Na Phosphate citrate pH 4.2, 0.2 M Li_2SO_4 and cryoprotected in the same solution supplemented with 33% ethylene glycol. Crystals of rA16/G9 in complex with VHH-D07, VHH-B01 and VHH-C05 were grown in 20% (w/v) PEG 3350, 0.2 M KH_2PO_4 and cryoprotected in the same solution supplemented with 33% ethylene glycol. Diffraction images were integrated with XDS (version 10 January 2022),[74] and crystallographic calculations were carried out with programs from the CCP4 program suite (version 9).[82] To determine the phases, we used AlphaFold (version 2)[68] models for A56^{IG}, K2 and the VHHs and the crystal structure of A16/G9 (PDB code: 8GP6[59]) as molecular replacement templates for PHASER (version 2.8.3).[62] To obtain the final models, we iteratively built and refined the structures using phenix.refine (version 1.19.2-4158)[61] and coot (version 0.9.8.95)[63] using isotropic B factor and TLS groups as refinement strategy. We validated all the models using MolProbity (version 4.5.2).[83] The crystallographic statistics and Protein Data Bank (PDB) codes are provided in Table S1.

Cryo-electron microscopy

Purified A16/G9/A56^{IG}/K2 complex was diluted to a concentration of 0.3 mg/mL in 10 mM Tris pH 8.0, 100 mM NaCl. Then, 4 μL of the complex was deposited on a UltrAufoil R1.2/1.3 300 mesh copper grids that had been glow-discharged for 25 seconds in the PELCO easyglow cleaning system. Excess protein was blotted away for 3 s using Whatman No.1 filter paper with a blot force of 0 at 15 °C in 100% humidity before being plunge frozen in liquid ethane using Vitrobot Mark IV (Thermo Fisher). The complex at pH 5.5 was assembled and purified in tri-component buffer (100mM Tris; 50mM MES; 50mM NaAc; 150mM NaCl pH5.5) and excess protein was blotted away 4 s. Frozen grids were imaged in a Titan Krios (Thermo Fisher Scientific) equipped with a Bioquantum K3 detector (Diamond) or TFS Falcon 4i (Soleil) operating in super-resolution mode at a magnification of 130,000 (Diamond) or 205,000 (Soleil), corresponding to a calibrated pixel size of 0,645 or 0.57 Å/pixel, respectively. A full description of the cryo-EM data-collection parameters is provided in Table S2.

Motion correction, contrast transfer function (CTF) estimation, particle picking, 2D classification, and non-uniform 3D refinement were performed using cryoSPARC (version 4.5.3).[64] For model building, the map was sharpened using DeepEMhancer (sbgrid version 20241203_5f64fe8_cu11),[66] and an initial model was generated via ChimeraX (version 1.6.1)[65] using the crystal structures of rA16/G9 and A56^{IG}/K2. The model was further built manually in Coot (version 0.9.8.95)[63] and refined iteratively using phenix.refine (version 1.19.2-4158)[61] using a refinement strategy that includes minimization_global, local_grid_search, and adp, with rotamer and Ramachandran restraints. Despite multiple rounds of building and refinement, the correlation coefficients of A16 and G9 were under 0.7, which were quite low.[84] An analysis of the distribution of the correlation coefficients (Figure S6) revealed that the values in the NTD and the interface with A56^{IG}/K2 are close to 0.8, while in the CTD regions, due to the worse resolution of the map, are on average below 0.6. To illustrate the quality of the map and the fitting in the interface, we have included snapshots of the map at sites A, B and C (Figure S6). The full cryo-EM data processing workflow is shown in Figure S6 and the model refinement statistics can be found in Table S2.

Bio-Layer Interferometry (BLI) measurements

All the BLI data showed in this manuscript have been produced using an Octet R8 (Sartorius, Gottingem, Germany). The BLI data shown in Figure 2 were generated as follows: A56^{IG}/K2 was biotinylated in the Avi-tag placed at the C-terminus of K2 (A56^{IG}/K2-BIO) using BirA biotin ligase (Avidity). Streptavidin (SA) sensors (Sartorius) were dipped into solution containing A56^{IG}/K2-BIO at 12.5 μg/mL, blocked for 300 seconds (sec) in PBS-BSA (1 mg/mL) supplemented by 200nM unrelated biotinylated protein and dipped into solutions of rA16/G9 diluted at different concentrations (450, 225, 112, 56, and 28 nM) and pHs (7.4, 6.5, 5.5, 4.5). Association and dissociation rates were recorded for 150 s (panel B) and 900sec (panel G). Non-specific interactions were monitored using a sensor coated with unrelated biotinylated protein and signals were subtracted. The data shown in Figure 4B were generated on Anti-Human-Heavy Chain (AHC) sensors (Sartorius) dipped respectively into VHH-Fc at 50 μg/mL or the bispecific antibodies at 18 μg/mL. After quenching for 300 seconds (sec) in PBS-BSA (1 mg/mL), sensors were dipped into solution containing rA16/G9 or rG9 at different concentrations (24, 12, 6, and 3 nM). Association and dissociation rates were monitored for 180 s. The curves were

processed using the Octet Analysis Studio software (version 13.0; Sartorius), and the K_D values were obtained after fitting to a 1:1 global model. K_D values are reported as the average from 3 independent experiments.

Serpin activity assay

For the serpin activity assay, we expressed the plasminogen activator inhibitor type-1 (PAI-1) with the mutation W175F and an N-terminal double strep-tag[85] in Escherichia coli BL21(DE3) cells (New England Biolabs). We induced protein expression overnight (o/n) at 16°C with 1 mM IPTG and purified the protein by affinity purification followed by SEC in PBS. We used the same protocol to express K2 in Escherichia coli BL21(DE3) cells ($K2^B$). $A56^{IG}$ and K2 ($K2^{S2}$) were produced in Drosophila S2 cells as described above. For the serpin activity assay, we used 200 nM $K2^B$, 200 nM $K2^{S2}$, 200nM PAI-1 (W175F), 600 nM $A56^{IG}$ and 300 nM urokinase-type plasminogen activator, uPA (Millipore). Samples were incubated at 37°C for 1 hr and complex formation was analyzed by SDS-PAGE and Western blot using an anti-Strep monoclonal antibody.

ELISA cross-competition assay

To determine the cross-competition among different VHHs, we performed inhibition binding assays. In detail, ELISA plates (NUNC-immuno 439454) were coated with 100 μL/well of A16/G9 at final concentration of 1 μg/mL in phosphate buffer saline (PBS) pH 7.4. After washing with 0.05% Tween-20 in PBS and blocking with milk buffer (5% dry-nonfat milk, 0,05% Tween-20 in PBS), we added 50 μl/well of VHH at 1 μM and incubated for 60 minutes at room temperature (RT). Then, we added 50 μL of dimeric IgG-VHH (B01, D07, and E12 at 1 nM, C05 at 0.5 nM) and incubated 90 minutes at RT. Plates were washed and binding revealed by adding HRP-conjugated goat anti-human IgG (Jackson ImmunoResearch) at final 1:10,000 dilution, followed by 1-StepTM Ultra TMB substrate. Color was allowed to develop for about 15 minutes and the reaction was stopped adding 0.18 M H_2SO_4. Absorbance at 450 nm was measured in the Infinite M1000 PRO microplate reader (Tecan). Data were analyzed using GraphPad Prism (version 10).

Generation of recombinant VACV

All recombinant VACV were constructed as previously described.[58] In brief, BSC-40 cells were infected with the parental viruses and subsequently transfected with linearized plasmid that contained the region of genome to be replaced and was flanked at its 5′ and 3′ ends by 300 bp of genomic sequence for targeted homologous recombination. Recombinant viruses were selected by fluorescence through four rounds of plaque purification.

VACV MV and EV production

To purify MVs, BSC-40 cells were infected with VACV-WR at MOI 1. After 24 h of incubation at 37°C, cells were harvested and subjected to Dounce homogenization. MV from cytosolic extracts were sedimented in a 36% sucrose cushion by centrifugation at 4°C for 80 min at 53,000 g and 4°C in a SW32 Ti Rotor (Beckman Coulter). The sedimented virus was recovered and resuspended in 10 mM Tris-HCl (pH 9). The virus titer was determined by plaque assay in BSC-40 cells in presence or absence of 1% guinea pig serum as a source of complement (GPC; Rockland). To produce EVs we followed a published protocol.[86] HeLa cells were infected at MOI 0.1 and virus was harvested from the supernatant 48 hours post infection. Cell debris were removed by centrifugation (450xg for 8 min at 4°C) and the clarified supernatant was aliquoted and stored at -80°C. Viral stocks were used after a single freeze–thaw cycle and tittered in the presence of an MV neutralizing anti-L1 antibody (7D11) at 50 μg/ml and 10% Baby Rabbit Complement (BRC; Cedarlane). The VACV IHDJ strain was obtained from the laboratory of Jason Mercer (University of Birmingham). To produce viral stocks, HeLa cells were infected at MOI 0.1 and 72 hs post infection the virus was harvested, clarified (450xg for 8 min at 4°C) and stored at -80°C. All experiments with VACV were conducted under BSL2 conditions.

MV 24-hr yield, plaque assay and particle/PFU ratio

Confluent BSC-40 cells were infected with the appropriate VACV viruses in 60 mm dishes at an MOI of 1 for 24 hrs. Cells were then scraped into PBS and harvested at 700 g for 5 min. The cell pellet was suspended in 100 μL 1 mM Tris pH 9.0 and subjected to three rounds of freeze thawing in liquid nitrogen. Plaque assays were performed by titrating harvested virus onto confluent monolayers of BSC-40 cells in 6-well plates. Cells were infected with 10-fold dilutions of VACV and incubated for 48 hr before being stained with 0.5% crystal violet in 2% PFA. For the particle/PFU ratio, 5 x 15 cm dishes were infected with sedimented virus at MOI 2 for 48 hrs. Virus was harvested and banded as previously described (Mercer and Helenius, 2008). Particle number was measured by light scattering at 260 nm (optical density (OD) value of 1 = 1.2×10^{10} particles).

Early gene expression determination by qRT-PCR

6-well plates of HeLa cells were infected with VACV at MOI 1 and incubated at 37°C. Cells were harvested 4 hpi and RNA was extracted according to the RNeasy Plus Mini kit (Qiagen) protocol. 500 ng of total RNA was used for cDNA synthesis with SuperScript reverse transcriptase (Thermo Fisher Scientific) and Oligo(dT) primer (Invitrogen). qPCR reactions were carried out using Mesa Blue qPCR MasterMix and the C11R primer (5′-AAACACACACTGAGAAACAGCATAAA-3′ and 5′-ACTATCGGCGAATGATCTGATTA-3′) on the BioRad CFX connect qPCR machine. Results were normalized against GAPDH expression.

Please cite this article in press as: Meola et al., Structural basis of poxvirus fusion regulation and anti-A16/G9 antibody-mediated neutralization and protection, Cell (2025), https://doi.org/10.1016/j.cell.2025.07.040

Virus induced cell-cell fusion (fusion from without assay)

BSC-40 cells were grown to confluency in 10-well CELLview slides (Greiner Bio-One). Recombinant VACV and VACV WT were bound to cells at MOI 50 PFU/cell for 1 hr at 4°C before washing twice with PBS followed by incubation at 37°C with 20 mM MES) adjusted to pH 5 or 7.4 for 5 min. Cells were washed with PBS and incubated with full medium for 2 hrs at 37°C. Cells were fixed, permeabilized with 0.1% Triton X-100 (Sigma-Aldrich) and stained with Alexa Fluor 594-phalloidin (1:1000, Invitrogen) and Hoechst-33258 (1:2000, Invitrogen) for 1 hr. Images were acquired with a VT-iSIM microscope (VisiTech) with a Plan Apo lambda 100X oil objective. AlexaFluor-594 fluorescence was excited with the 561 nm laser and Hoechst with the 405 nm laser. The fusion index was calculated using the formula: f = [1-(C/N)] where f is the fusion index, C is the number of cells and N is the number of nuclei.

For the fusion inhibition assay with mAbs (Figure 6B) BSC-40 cells were plated at 2×10^4 cells per well in a μClear 96-well plate (Greiner Bio-One). The following day, 1×10^6 PFU of WT VACV-WR (MV stock) were mixed with 10-fold serial dilution of mAbs and added onto the cell monolayer. After 1 hr incubation at 4°C, the fusion assay and cell staining were performed as described above. Images were acquired with an Opera Phenix high-content confocal microscope (Perkin – Elmer) using a 20X immersion objective. AlexaFluor-594 fluorescence was excited with the 561 nm laser and Hoechst with the 425 nm laser. Fifteen fields per well were acquired and image analysis was automated with a custom Python script based on Cellpose-SAM model[87,88] (https://pypi.org/project/cellpose/) and scikit-image library[89] (https://scikit-image.org/).

MPXV neutralization assay

The neutralization assay was previously described.[75] U2OS cells were plated at 8×10^3 cells per well in a μClear 96-well plate (Greiner Bio- One). The following day, in a BSL-3 facility each virus was incubated with 1% of human serum as a source of complement (pool of two non-neutralizing sera) and serial dilutions of monoclonal antibody. After two hours, the mix were added to the cells. The viral inoculum was determined to obtain a non-saturating infection.[3,75] Forty-eight hours later, cells were fixed for 30 min at room temperature (RT) with 4% paraformaldehyde (PFA, Electron Microscopy Sciences), washed and immunostained for MPXV antigens with rabbit polyclonal anti-VACV antibodies (PA1-7258, Invitrogen), and an Alexa Fluor 488-coupled goat anti-rabbit antibody (Invitrogen). Nuclei were stained with Hoechst (1:10,000; Invitrogen). Images were acquired with an Opera Phenix high-content confocal microscope (PerkinElmer). For each condition, infection was quantified by calculating the total area of MPXV-positive cells (MPXV+ area) and the nuclei were counted using the Harmony software (PerkinElmer). The percentage of infection inhibition was calculated from the MPXV+ area using the following formula:

$$100 * \left[1 - \left[\frac{(MPXV^{+}\ area\ with\ Antibody) - (mean\ area\ of'non - infected'controls)}{(mean\ area\ of'no\ antibody'\ infected\ controls) - (mean\ area\ of'non - infected'controls)}\right]\right]$$

Inhibition activity of each antibody was expressed as the IC50 (Half-maximal inhibitory concentration). IC50 were calculated based on an inhibitory dose-response curves with a variable slope model, using the percentage of inhibition at the different antibody concentrations.

VACV neutralization assay

BSC-40 cells were plated at 2×10^4 cells per well in a μClear 96-well plate (Greiner Bio-One). 300 PFU of VACV-WR MV or VACV-WR EV were mixed (ratio 1:1) with serial dilutions of mAbs in the presence or absence of 1% guinea pig serum as a source of complement (Rockland) for MV and 10% Baby Rabbit Complement (Cedarlane) for EV. For EV, 50 μg/ml of 7D11 was also added to the mixture to deplete the MV particles or damaged EV. After incubation for 2 h at 37°C, the mixture was added onto BSC-40 cell monolayers. Twenty-four hours later, cells were fixed for 30 min at room temperature (RT) with 4% PFA. Images were acquired with a FluoroSpot (InmunoSpot, CTL). The number of green foci was quantified using the FluoroSpot proprietary software and the percentage of neutralization was calculated as follow: 100 – 100 x (N – Nn)/(Np – Nn) where N is the number of foci in the treatment, Nn is the number of spots detected in non-infected cells and Np is the number of foci detected in non-treated infected cells. Neutralizing activity of each mAb was expressed as the IC50 (effective dose inhibiting 50% of infection). IC50 values were calculated using a reconstructed curve with the percentage of neutralization at the antibody concentrations using PRISM software (Version 10.2.1).

Adsorption inhibition assay

BSC-40 cells were plated at 2.5×10^5 cells per well in a Costar 12-well plate (Corning Inc.). The following day, 2.5×10^5 PFU of VACV-WR MV were mixed with serial dilutions of mAbs. After the incubation for 2 h at 4°C, the mixture was added to the cell monolayers (500 μl) and the virus was allowed to bound to cells for 2 h at 4°C before washing three times with PBS. The total DNA of the sample was extracted using the DNeasy Blood & Tissue kit (Qiagen) following the manufacturer's instructions for cultured cells. The number of genome copies of the adsorbed virus was quantified by qPCR using the iTaq Universal SYBR Green Supermix (Bio Rad) and the C11R primer (5′-AAACACACACTGAGAAACAGCATAAA-3′ and 5′-ACTATCGGCGAATGATCTGATTA-3′) on the QuantStudio 6 Flex System qPCR machine (Thermo Fisher Scientific). To determine the absolute number of genomes copies we used the NanoDrop quantified plasmid pT350-C11R, which includes the C11R VACV gene sequence, to build a standard curve. Data analysis was done using the QuantStudio Real Time PCR software.

Comet inhibition assay

BSC-40 cells were plated at 2.5 × 10^5 cells per well in a Costar 12-well plate (Corning Inc.). The following day, cells were infected with 30 PFU/well of VACV-IHDJ. After the incubation for 2 h at 37°C, the virus inoculum was removed, and cells were treated with 10 μg/ml of mAb and incubated for 56 h at 37°C. Cells were fixed with PFA 4% and stained with 0.5% crystal violet in 2% PFA. Images were acquired with an EliSpot (InmunoSpot, CTL) using the BioSpot suit.

Analysis of VACV virus yields by plaque assay

To quantify VACV infectious titers, undiluted and serial ten-fold dilutions of homogenized lung tissues were prepared and added in triplicate to BSC-40 cell monolayers seeded in 12-well plates at a density of 5 x 10^5 cells per well. After 1 hour of adsorption at 37°C with 5% CO_2, the inoculum was removed, and the plates were incubated at 37°C with 5% CO_2 in DMEM supplemented with 2% FBS. After 48 hours, cells were fixed with 10% formaldehyde (Sigma-Aldrich) for 1 hour and subsequently stained with 0.5% crystal violet (Sigma-Aldrich). Viral plaques were visualized and counted, and VACV titers were expressed as PFUs/g of lung tissue.

RNA isolation and quantification of VACV by reverse transcription-quantitative polymerase chain reaction (RT-qPCR)

To assess VACV mRNA expression viral mRNA levels were quantified in homogenized lung tissues. VACV viral mRNA detection was performed using a previous validated probe set for VACV mRNA quantification.[90] Gene expression levels were normalized to the 28S ribosomal RNA gene. First-strand cDNA synthesis and subsequent real-time PCR were performed using NZYSpeedy One-step RT-qPCR Master Mix (NZYTech) following the manufacturer's specifications, with ROX as the reference dye. RT-qPCR was carried out using TaqMan probes (Thermo Fisher Scientific; sequences available upon request). mRNA levels were quantified as arbitrary units (A.U.) relative to uninfected control samples (negative RNA controls from uninfected cell cultures or mice) using the 2-ΔΔCt method. All samples were analyzed in duplicates to ensure reproducibility.

Molecular dynamic simulations

For the molecular dynamics simulations, we employed the AMBER-ff14sb force field.[91] Two myristic acid molecules (tetradecanoic acid), predicted by AlphaFold3[26] to bind in the NTD of A16/G9, were manually linked to their respective N-termini. The GAFF-2.11[92] force field parameters with AM1-BCC charges were derived for myristic aldehyde (tetradecanal) using the TOFF[69] software. A new residue (MGLY), representing the linkage between myristic aldehyde and glycine, was incorporated into the force field. This linkage formed a novel peptide bond, for which bonded parameters were inferred from the AMBER-ff14sb1 force field. The charge of the carbonyl hydrogen of myristic aldehyde was transferred to its corresponding carbonyl group upon peptide bond formation, with the hydrogen subsequently removed from the structure. The TIP3P[93] water model was utilized, alongside AMBER ion parameters. Classical molecular dynamics simulations were conducted using the GROMACS-2022.4 package.[70] An electrically neutral and solvated system with 150 mM of NaCl was created in an octahedron box with 1.5 nm distance between the solute and the box surface using the solvate module of GROMACS.

The system temperature was maintained at 298.15 K using the velocity-rescale thermostat[94] with a time constant of 1 ps. For constant-pressure simulations, an isotropic stochastic cell rescaling barostat (c-rescale)[95] was applied to maintain a pressure of 1 bar with a time constant of 5 ps. Van der Waals and electrostatic interactions were treated using the cutoff and Particle Mesh Ewald (PME) methods,[96,97] respectively, with a real-space cutoff radius of 1 nm. Hydrogen bonds were constrained via the Lincs algorithm,[71] and a hydrogen mass repartitioning factor of 2.5 was used, enabling a 4 fs integration time step for production simulations. Additional molecular dynamics parameters are detailed in the GROMACS input files provided as Supplementary information

The system was energy-minimized using the steepest-descent algorithm, applying position restraints on heavy atoms with a force constant of 2000 kJ/mol/nm^2. Next, two 125 ps NVT equilibration steps were carried out, each employing a 1 fs integration time step and position restraints of 4000 and 2000 kJ/mol/nm^2 respectively. Subsequent equilibration involved a 125 ps NPT phase using the c-rescale barostat, reducing the restraint force constant to 1000 kJ/mol/nm^2. Three additional NPT steps of 500 ps, 500 ps, and 1 ns followed, employing a 2 fs integration time step with force constants of 500, 200, and 50 kJ/mol/nm^2, respectively. Restraints were then removed in two further NPT steps: the first lasting 1.5 ns with a 3 fs integration time step, and the second lasting 10 ns with a 4 fs time step.

Production simulations were performed on ten independent replicas of the equilibrated structure with NPT conditions, each running for 200 ns with a 4 fs integration time step, achieving a cumulative sampling of 2 μs. Random velocities were independently assigned to each replica at the start of the simulations. Trajectories were recorded at 100 ps intervals, producing 2001 frames per simulation.

The distance between the center of mass of the two MGLY residues and the center of mass of the backbone atoms within 0.4 nm (as defined in the first reference frame) was calculated for all simulation frames. Additionally, the root-mean-square deviation (rmsd) of the two MGLY residues was monitored throughout the concatenated trajectory, which was pre-aligned to the backbone atoms.

In vivo evaluation in mice of the protective efficacy of the A56/K2-C05-Fc antibody against VACV

To assess the protective efficacy of the bispecific antibody A56/K2-C05-Fc, female C57BL/6 mice (8 weeks old at the start of the study) were randomly assigned into treatment and control groups (n = 10 per group). Mice in the treatment group received 100 μg of A56/K2-C05-Fc antibody via intraperitoneal injection (in 200 μL of PBS) one day prior to VACV WR challenge. Control groups

received either an irrelevant IgG1 control antibody or PBS using the same administration route and volume. At day 0, mice immunized with A56/K2-C05-Fc antibody, the irrelevant IgG1 or PBS were challenged intranasally with 1×10^6 PFUs of VACV WR strain in 25 μL of PBS, under isoflurane anesthesia. Control naive mice were inoculated with PBS. Following infection, mice were monitored daily for clinical signs, body weight loss, and survival for 6 days. Mice that lost more than 25% of their initial body weight or showed severe disease signs were humanely euthanized. At day 5 post-challenge, 5 mice per group were euthanized, and lung tissue samples were collected for analysis. The right lung lobe was divided: one part preserved in RNAlater (Sigma-Aldrich) at -80°C for RNA extraction, and the other part frozen for virus titration. Lungs were homogenized respectively in 2 mL of RLT buffer (Qiagen) with β-mercaptoethanol or 1X PBS using a gentleMACS dissociator (Miltenyi Biotec). Infectious virus titers were quantified by standard plaque assay on BSC-40 cells, and viral genome copies were quantified by qRT-PCR using primers targeting the VACV CrmB gene.

Mice immunization with rA16/G9 and evaluation of the protective efficacy against VACV

To evaluate the protective efficacy of rA16/G9, female C57BL/6 mice (14 weeks old, $n = 10$ per group) were randomly assigned into experimental groups and vaccinated via intramuscular injection in the quadriceps muscle at weeks 0 and 3. The groups received: i) rA16/G9: 10 μg per mouse formulated in a 1:1 (v/v) ratio with Alum adjuvant (Alhydrogel, InvivoGen) (group 1); ii) B5 ectodomain: 10 μg per mouse, also adjuvanted with Alum (1:1) (group 2); iii) MVA: 1×10^7 PFUs per mouse diluted in PBS (group 3); and iv) Mock (PBS): negative control (groups 4 and 5). At week 6, mice were challenged intranasally under light isoflurane anesthesia with 1×10^6 PFUs of VACV WR strain in 25 μL PBS. Mice of group 5 were inoculated with PBS, as a negative control of infection. Following infection, mice were monitored daily for body weight loss and clinical signs of disease for 37 days. Mice that lost more than 25% of their initial body weight or showed severe disease signs were humanely euthanized. At day 5 post-challenge, 5 mice per group were euthanized, and lung tissue samples were collected for analysis. Mice lungs were analyzed for viral replication as indicated in the previous experiment.

Serology studies (ELISA)

The levels of A16/G9- or MVA-specific IgG in serum samples from immunized mice were measured using homemade ELISA at CNB-CSIC. Briefly, 96-well ELISA plates (ThermoFisher) were coated with 5 μg/well of purified A16/G9 protein or MVA cell extract in sodium carbonate at 4°C overnight. Subsequently, serial 2.5-fold dilutions of mouse serum samples were prepared, starting at a 1:100 dilution, in PBS containing 1% milk and 0.05% Tween-20. After blocking plates with 5% milk and 0.05% Tween in PBS for 2 hr at RT, diluted sera were added for 1.5 hr at RT. Plates were washed 3 times in PBS-Tween 0.05% and were then incubated for 1 hr at RT with HRP-goat anti-human IgG (1 μg/mL, ThermoFisher, Cat. No. H17000) in 1% milk and 0.05% Tween in PBS. Plates were washed and the TMB substrate (Sigma-Aldrich) was added, and the reaction was stopped by adding 1M H_2SO_4. Absorbance was read at 450 nm. Total IgG titer was measured as the last dilution that gives an absorbance at least 3 times higher the absorbance of a naïve serum.

The levels of B5-, A33- or A16/G9- specific IgG in human sera were measured using homemade ELISA at Necker hospital. Briefly, 96-well ELISA plates (ThermoFisher) were coated with 250 ng/well of purified B5, A33 or A16/G9 protein in sodium carbonate at 4°C overnight. Human sera were treated with 1% Triton X-100 for 1 hr and subsequently diluted at 1:100, 1:300 and 1:900. After blocking plates with 5% milk and 0.05% Tween in PBS for 1 hr at RT, diluted sera were added for 1 hr at RT. Plates were washed 5 times in PBS-Tween 0.05% and were then incubated for 1 hr at RT with HRP-goat anti-human IgG (1 μg/ml, ThermoFisher, cat. No. H17000) in blocking buffer. Plates were washed 5 times in PBS-Tween 0.05% and incubated with KPL SureBlue™ TMB microwell peroxidase substrate (Eurobio, cat. No. 5120-0077) for 5 min at RT. The reaction was stopped by adding 1.8 N H_2SO_4, and optical density was measured at wavelengths of 450 and 620 nm. Results were normalized between plates using a common control pool of sera from immunized patients (2-fold serial dilutions, from 1:100 to 1:3200) to perform a standard curve on each plate and two blank wells were always added on each plate to control for background signal. Background-subtracted signal from each sample wells are first normalized as percentage of the control pool using the standard curve on each plate and the average result for the three dilutions for each sample was kept after excluding values outside the standard curve range. Final normalized results (Normalized ELISA value) are reported in Figure 7E. The positivity threshold was set at the 95th percentile of the control group (born after 1980).

Structure, and sequences analysis

Multiple sequence alignments showed in Figures S1, S3, and S4 were done using the ESPript server (https://espript.ibcp.fr).[60] Analysis of structures and representations were done using Chimera[65] and Pymol (Schrodinger, LLC). Software used in this project was curated by SBGrid.[67]

QUANTIFICATION AND STATISTICAL ANALYSIS

Statistical details, including the number of replicates (n), measures of precision, and the statistical test used for each experiment can be found in the corresponding figure legends. All graphical representations, calculations, and statistical analyses were performed using GraphPad Prism software version 10.2.1 (GraphPad Software, San Diego, CA, USA).

CellPress
OPEN ACCESS

Supplemental figures

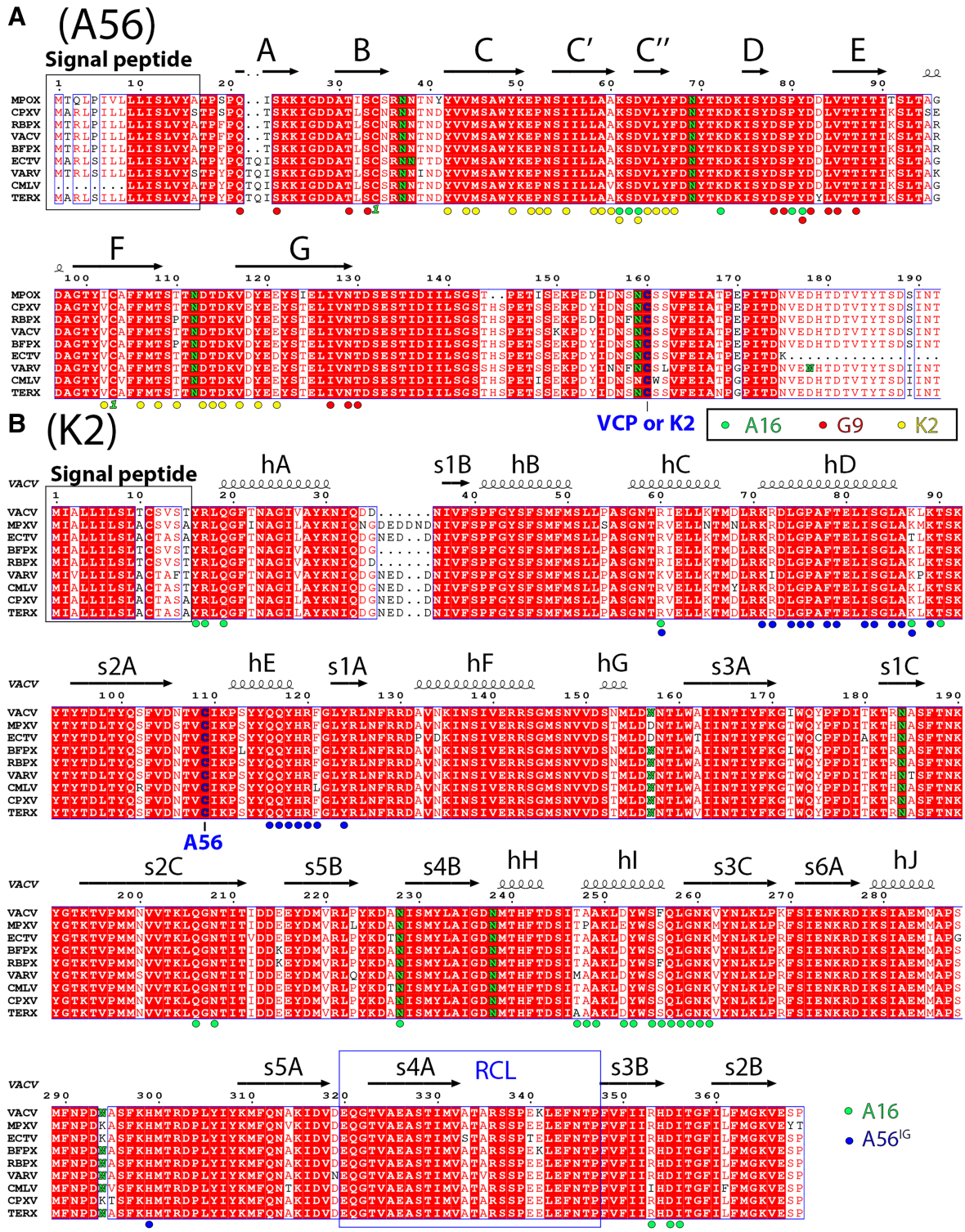

(legend on next page)

Figure S1. Sequence alignment of A56 and K2 across OPXVs, related to Figure 1

(A) Alignment of A56 sequences: MPXV (UniProt code: Q8BEJ5), cowpox virus (CPXV, Q6UN41), rabbitpox virus (RABP, Q8BEJ2), VACV (Q01218), buffalopox virus (BFPX, A0A2P1JPY1), ectromelia virus (ECTV, Q9YN65), variola major virus (VARV, Q8AYZ8), camelpox virus (CMLV, Q2TFV6), and taterapox virus (TATV, Q8BEJ7). Asparagines (N) forming part of an N-glycosylation motif are highlighted in green, and the free cysteine (C) is in blue. Residues contacting A16, G9, and K2 are indicated with colored circles.

(B) Alignment of K2 sequences: VACV (A0A2I2MBX0), MPXV (A0A7H0DN13), ECTV (O11455), BFPX (A0A2P1JPL3), RBPX (Q6RZR6), VARV (P33831), CMLV (A0A0K1LDD0), CPXV (A0A212PSG1), and TATV (Q0NPH5). Residues contacting A16 and A56 are indicated with colored circles under the sequences.

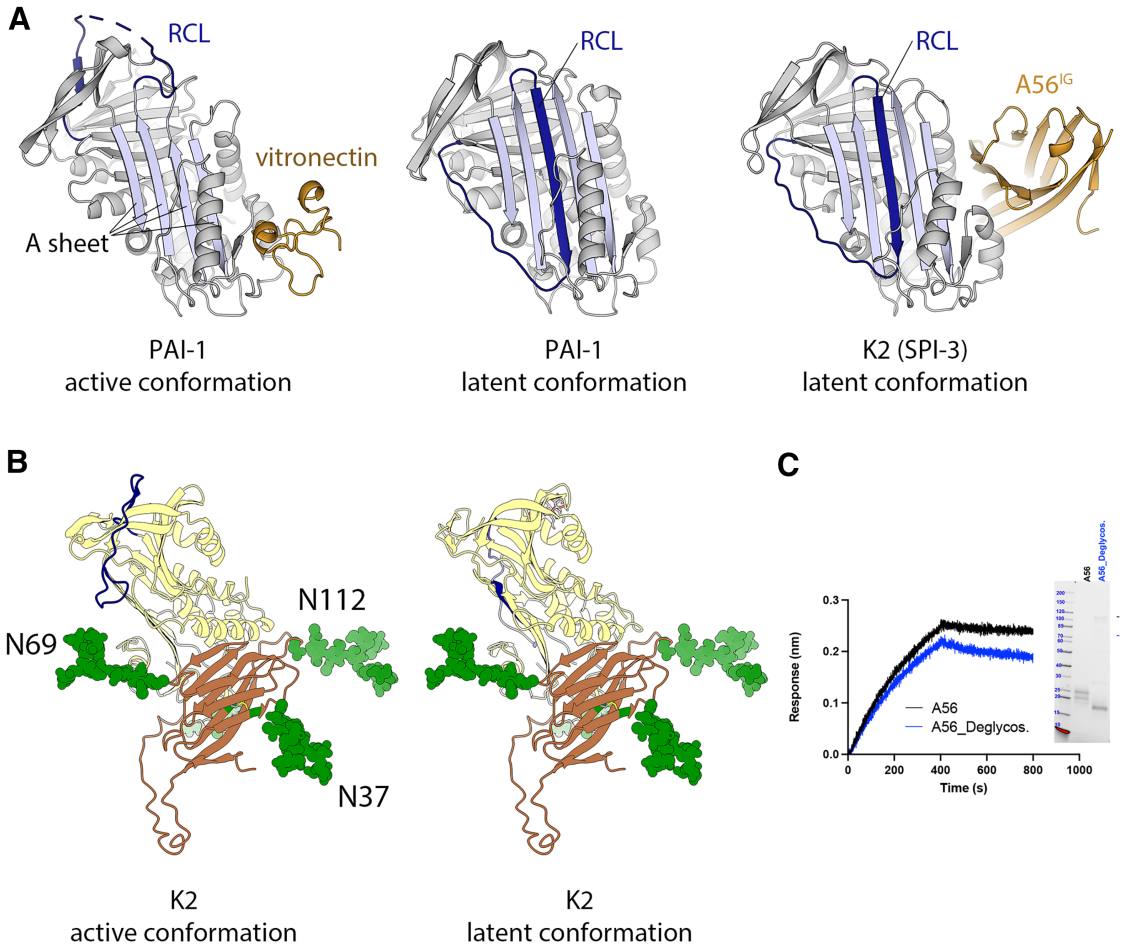

Figure S2. Structural analysis of K2 and A56, related to Figure 1

(A) Structural comparison of PAI-1 and K2. The left panel is a model of the complex formed by vitronectin and PAI-1 in its active conformation (PDB: 1OC0). The central panel presents a model of PAI-1 in the latent conformation (PDB: 1LJ5). The right panel shows a model of the A56^{IG}/K2 complex. The serpins are colored gray, the A-sheet in light blue, and the RCLs in dark blue. Vitronectin and A56^{IG} are colored in orange.

(B) Structural modeling of the three conserved N-glycans of A56^{IG}. The N-glycans are shown in green and labeled. The left panel displays a model of A56^{IG}/K2, with the serpin in the active conformation, and the right panel presents the crystal structure of the complex in the latent conformation.

(C) BLI-sensorgrams showing the interaction of glycosylated A56^{IG} (black curve) and deglycosylated (blue curve) with K2 at 50 nM.

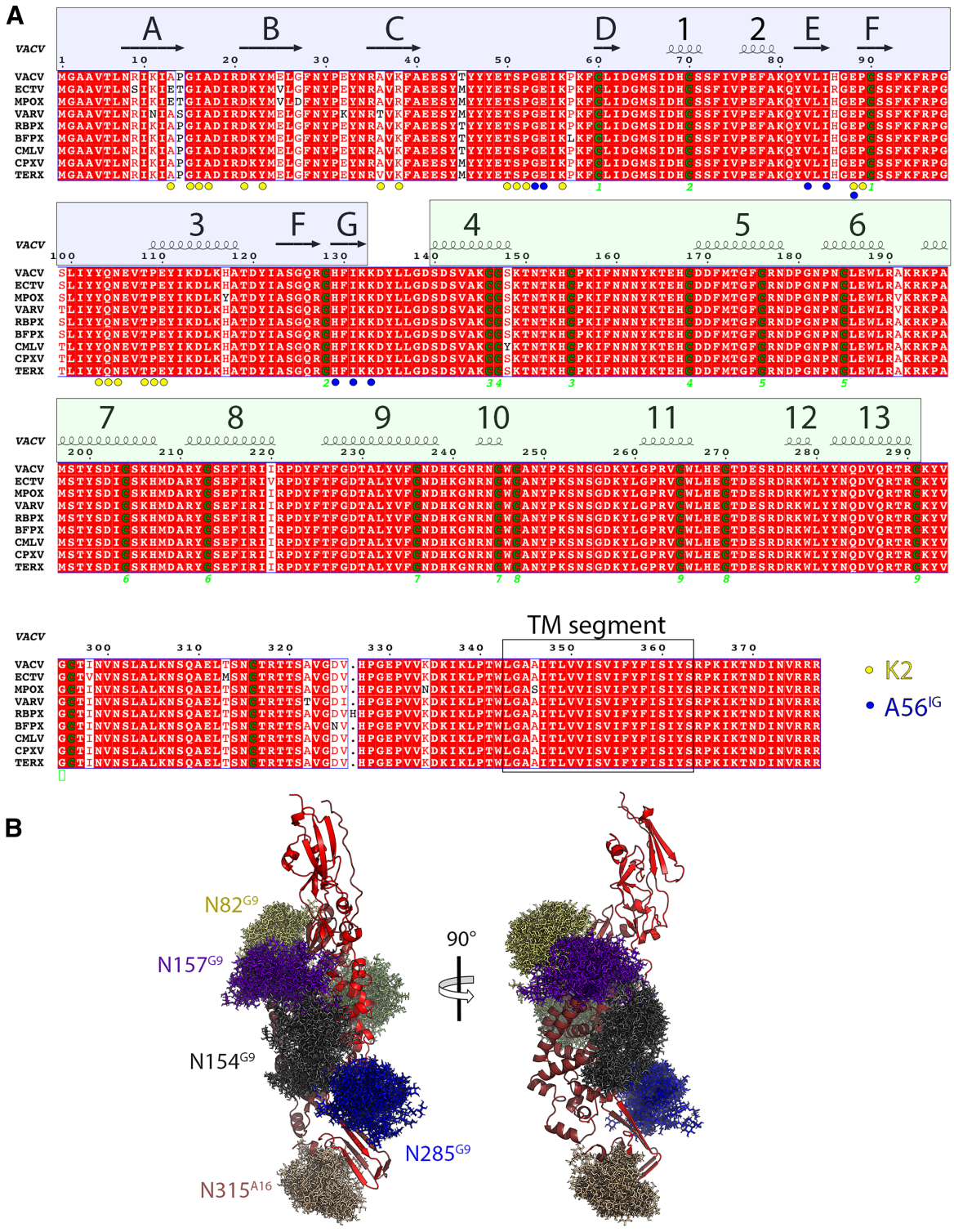

Figure S3. Sequence analysis of A16, related to Figure 2

(A) Sequences used in the alignment are from VACV (P16710), ECTV (NP_671638.1), MPXV (A0A7H0DNB5), VARV (P33841), RBPX (Q6RZG6), BFPX (WCS73424.1), CMLV (NP_570524.1), CPXV (ADZ24145), and TATV (YP_717445.1). Cysteines are highlighted in green, and disulfide bonds are labeled. Residues contacting K2 and A56 in the quaternary complex are indicated with colored circles under the sequences.

(B) Structure of A16/G9 with glycan conformers generated with GlycoSHIELD[73] to show the level of glycan masking.

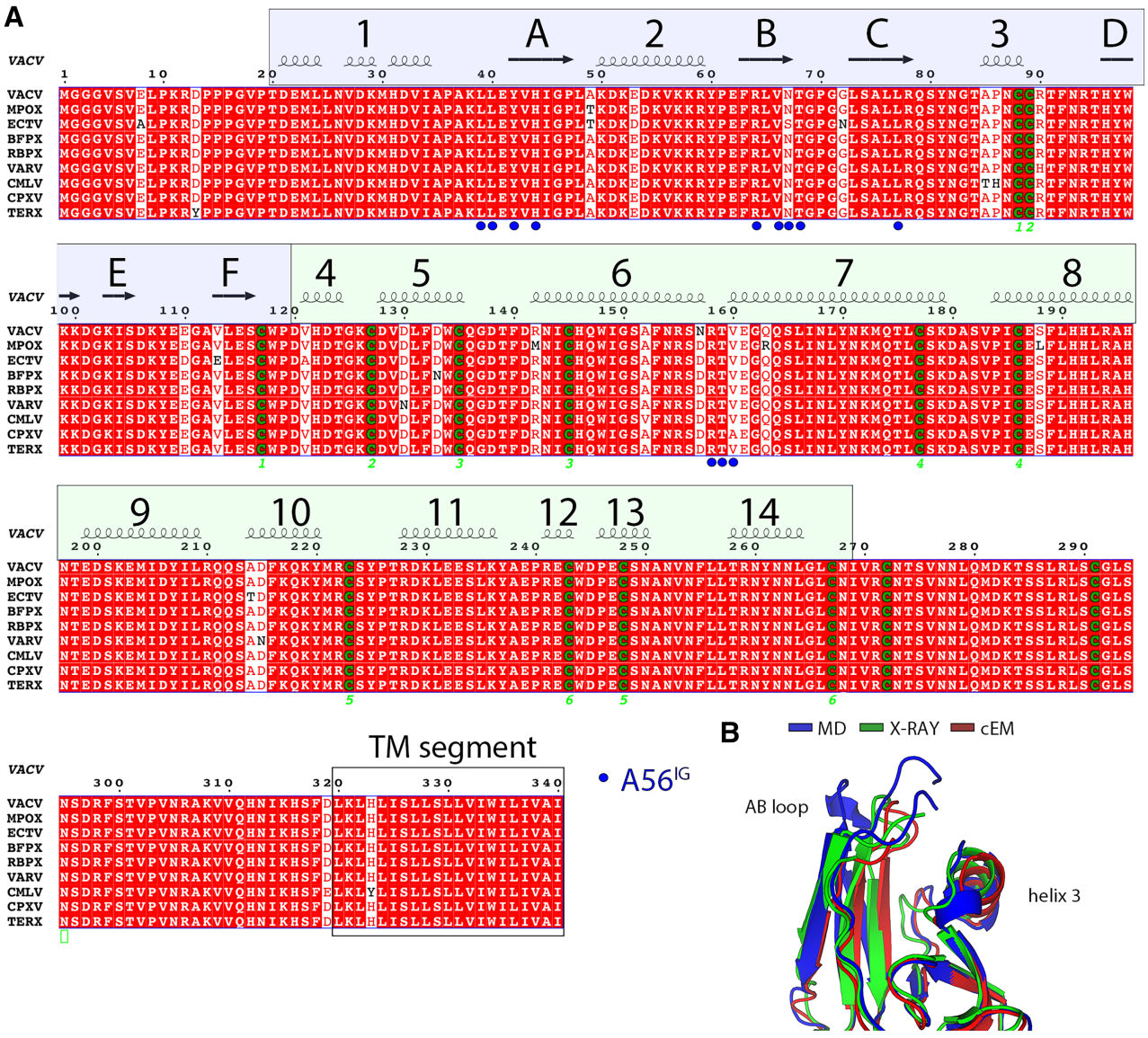

Figure S4. Sequence alignment of G9 across orthopoxviruses, related to Figure 3

(A) Sequences used in the alignment are from VACV (P07611), MPXV (NP_536506.1), ECTV (NP_671589.1), BFPX (AVO21101.1), RBPX (AAS49789.1), VARV (NP_042116.1), CMLV (NP_570475.1), CPXV (AGY97516.1), and TATV (YP_717397.1). Secondary structure elements and the transmembrane segment are indicated and labeled. Cysteines are highlighted in green, and disulfide bonds are labeled. Residues contacting A56 in the quaternary complex are indicated with blue circles under the sequences.

(B) Comparison of the A16^{NTD} region of MD, cryo-EM, and X-ray crystallography models.

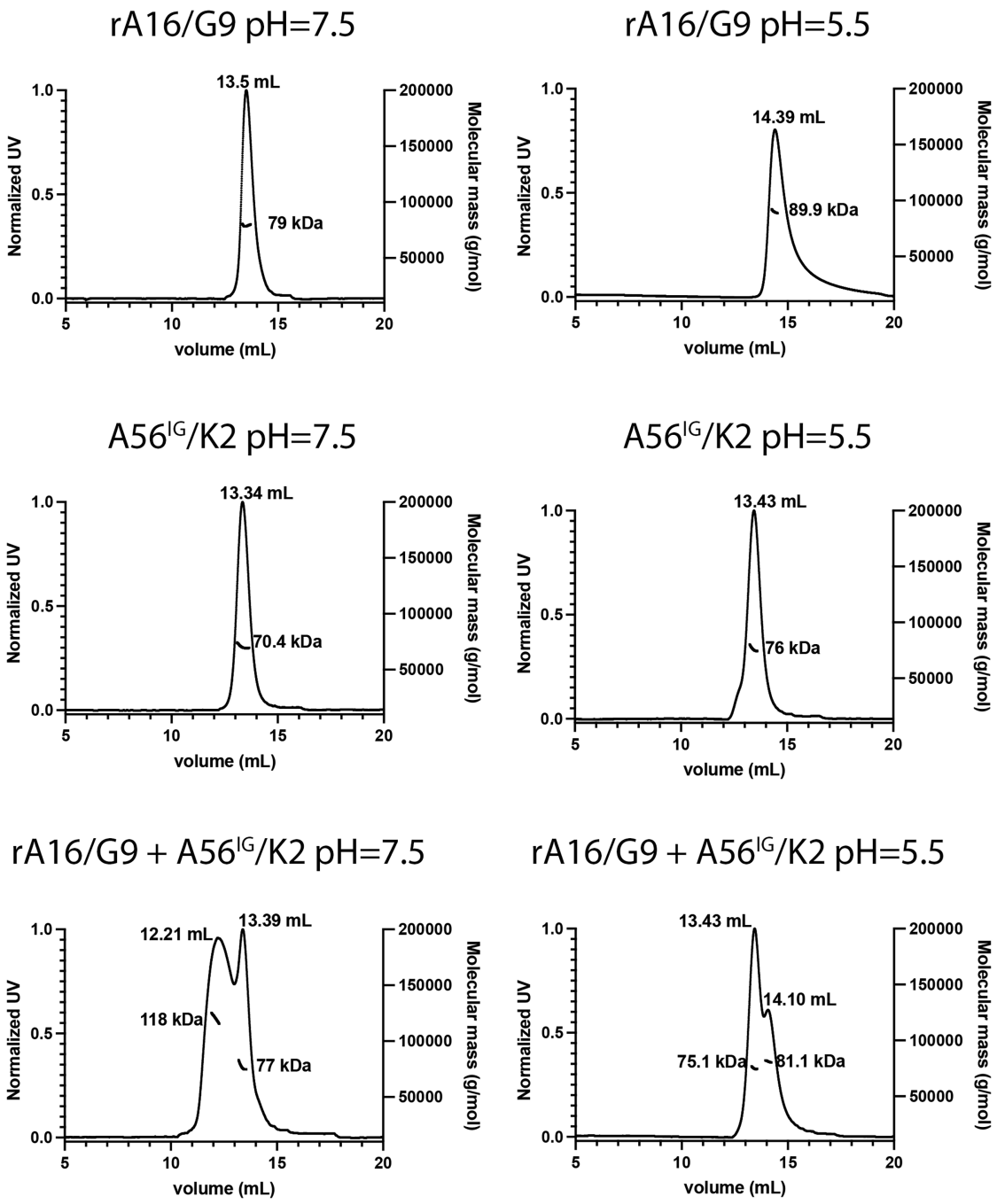

Figure S5. Biochemical characterization of A56^{IG}/K2 and rA16/G9 complexes, related to Figure 2

SEC-MALS analysis of rA16/G9, A56^{IG}/K2, and a mixture of both at pHs 7.5 and 5.5, as indicated.

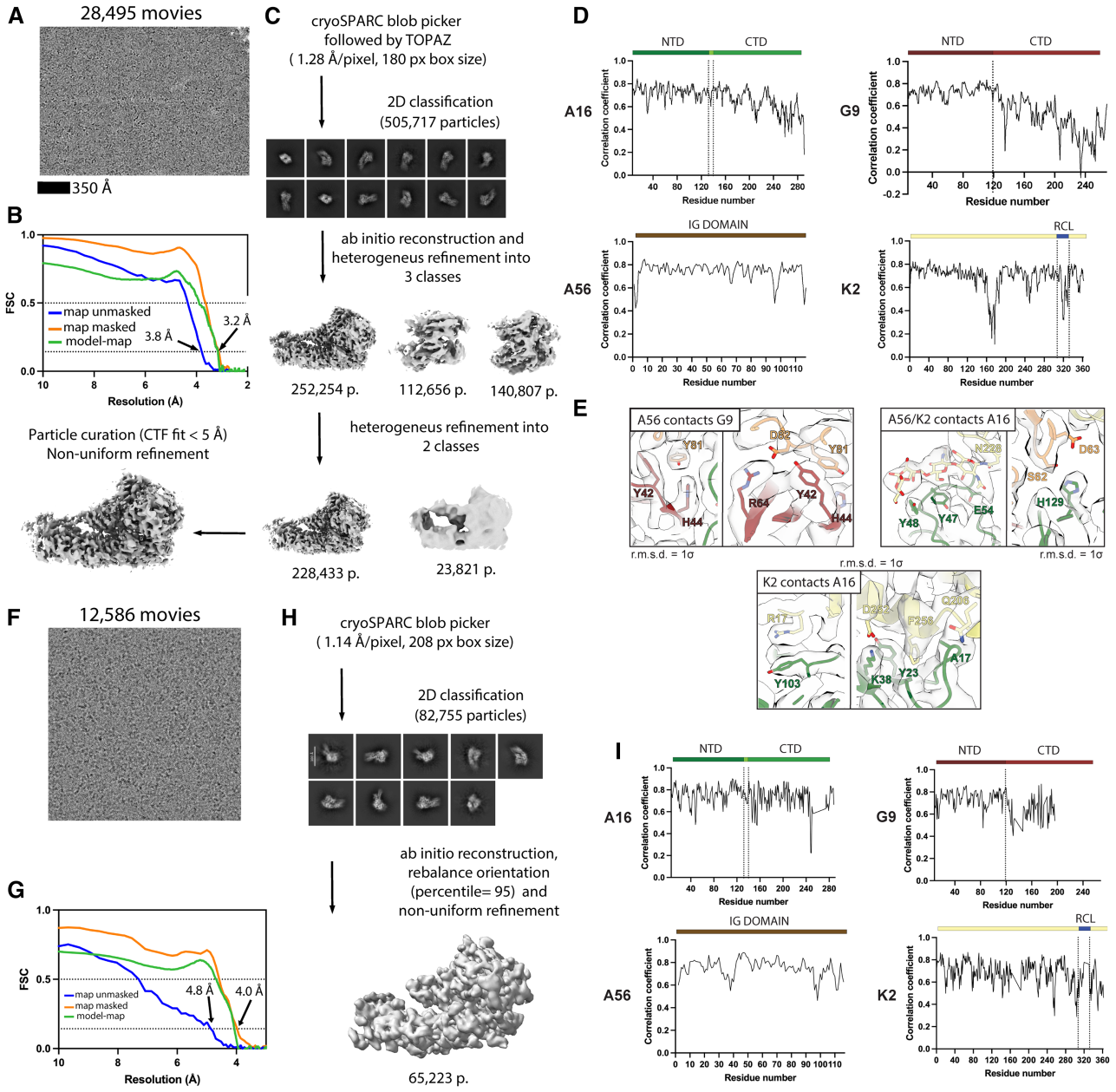

Figure S6. Cryo-EM image processing workflow and quality control, related to Figure 2

(A–E) Refers to the cryo-EM processing at neutral pH (7.5), and (F–I) at acidic pH (5.5).

(A and F) Representative micrograph used in processing.

(B and G) Fourier shell correlation (FSC) curves for the final map with (orange) and without (blue) mask, and model-map FSC curve (green).

(C and H) Data processing workflow used to obtain the final map.

(D and I) Correlation coefficient (CC) value plotted along the protein sequence of each chain.

(E) Close-up view of the interaction interface within the quaternary complex, and the residues are indicated, and the cryo-EM map is contoured at 1σ as indicated.

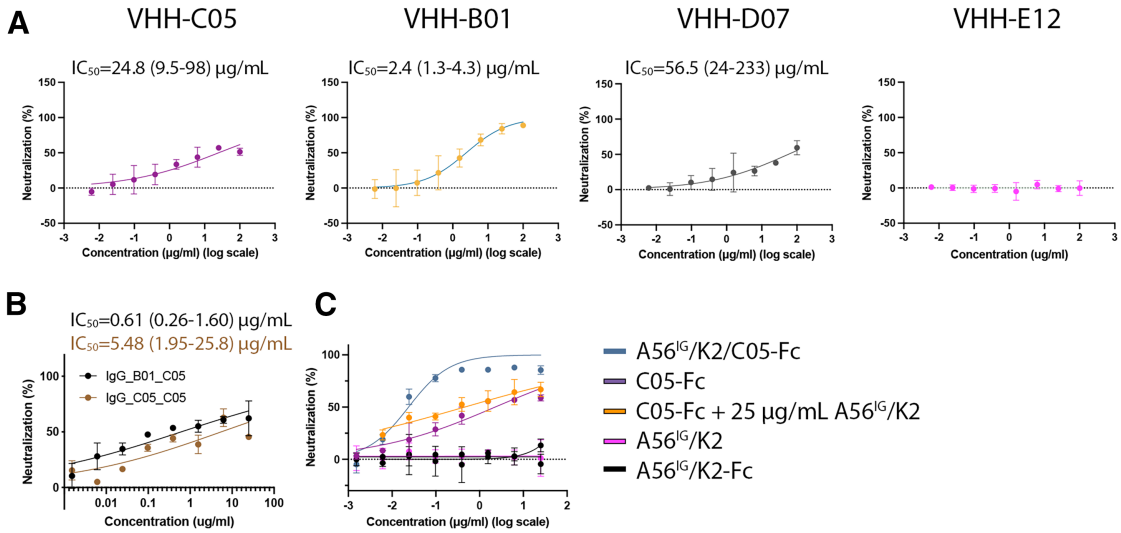

Figure S7. Monomeric VHHs neutralize VACV, related to Figures 4 and 5

(A) Neutralization assays of the four monomeric VHHs without complement using VACV-MVs. Data are the mean and 95% CI of triplicate wells from three independent experiments (n = 3).

(B) VACV neutralization assays using the tetravalent antibodies B01/C05 (black) and C05/C05 (brown) in the absence of complement. Data are presented as the mean ± SD of triplicate wells from three independent experiments (n = 3).

(C) Cooperative mechanism of A56^{IG}/K2/C05-Fc. Neutralization assays comparing the activities of bispecific antibody (A56^{IG}/K2/C05-Fc), C05-Fc, and C05-Fc in the presence of excess monomeric A56^{IG}/K2, monomeric A56^{IG}/K2, and the bivalent A56^{IG}/K2-Fc, as indicated in the legend. Data are presented as mean values ± SD.